

Soft X-Ray Spectrometers for Laser Driven Backlighter Experiments

Spektrometer für weiche Röntgenstrahlung aus laser-getriebenen Quellen

Master Thesis by Carlos Butler

Date: October 11, 2023

1. Review: Prof. Dr. Vincent Bagnoud
Darmstadt



TECHNISCHE
UNIVERSITÄT
DARMSTADT

Physics Department
Institute of Nuclear Physics
Working Group Bagnoud

Soft X-Ray Spectrometers for Laser Driven Backlighter Experiments
Spektrometer für weiche Röntgenstrahlung aus laser-getriebenen Quellen

Master Thesis by Carlos Butler

Date: October 11, 2023

Darmstadt

Erklärung zur Abschlussarbeit gemäß § 22 Abs. 7 und § 23 Abs. 7 APB der TU Darmstadt

Hiermit versichere ich, Carlos Butler, die vorliegende Master Thesis ohne Hilfe Dritter und nur mit den angegebenen Quellen und Hilfsmitteln angefertigt zu haben. Alle Stellen, die Quellen entnommen wurden, sind als solche kenntlich gemacht worden. Diese Arbeit hat in gleicher oder ähnlicher Form noch keiner Prüfungsbehörde vorgelegen.

Mir ist bekannt, dass im Fall eines Plagiats (§ 38 Abs. 2 APB) ein Täuschungsversuch vorliegt, der dazu führt, dass die Arbeit mit 5,0 bewertet und damit ein Prüfungsversuch verbraucht wird. Abschlussarbeiten dürfen nur einmal wiederholt werden.

Bei der abgegebenen Thesis stimmen die schriftliche und die zur Archivierung eingereichte elektronische Fassung gemäß § 23 Abs. 7 APB überein.

Bei einer Thesis des Fachbereichs Architektur entspricht die eingereichte elektronische Fassung dem vorgestellten Modell und den vorgelegten Plänen.

Darmstadt,

C. Butler

Contents

1. Introduction	7
2. X-Ray Absorption Fine Spectroscopy	11
3. Fundamentals of X-Ray Spectrometers	15
3.1. Flat Crystal Geometries	16
3.2. Bent Crystal Geometries	16
3.2.1. Von Hamos	17
3.2.2. Focusing Spectrograph with Spatial Resolution	17
3.3. Dispersion Calculation	19
3.4. Resolution	23
4. Spectrometer Design	25
4.1. Design Considerations	25
4.2. Implemented Spectrometer Schemes	27
4.2.1. Dual Unbent Crystal Spectrometer	28
4.2.2. Focusing Spectrograph with Spatial Resolution	29
4.2.3. Single Unbent Crystal Spectrometer	30
4.3. Specifications and Comparison	31
5. Experimental Setup	35
5.1. General Setup	35
5.2. Mechanical Design of Spectrometers	38
5.2.1. Dual Unbent Crystal Spectrometer	39
5.2.2. Focusing Spectrograph with Spatial Resolution	41
6. Data Analysis	45
6.1. Qualitative Performance	47
6.1.1. X-ray Emission Spectra	47
6.1.2. Absorption Spectra	50
6.2. Spectrometer Characterization	53
6.2.1. Spectral Resolution	53
6.2.2. Integrated Reflectivity Ratio	58
6.3. Setup Validation	60
6.3.1. Conversion Efficiency of He- α Line of Aluminum	60
6.3.2. He- α and Ly- α Line Ratio of Aluminum	61
7. Results and Discussion	63

8. Outlook	65
Bibliography	67
Appendices	70
I. Crystals	71
II. Calculations and Simulations	73
i. Simple Ray Tracing of the Focusing Spectrograph with Spatial Resolution	73
ii. Simulation of the Focusing Spectrograph with Spatial Resolution	75
iii. Simulation of the Dual Unbent Crystal Spectrometer	77
iv. Summary of Simulation Results	80
III. Alignment Procedure for FSSR-1D	81

1. Introduction

STILL THE EXACT SAME AS IN PROPOSAL. PARTS WILL BE ADDED/REWRITTEN IN THE FUTURE.

The experimental study of warm dense matter (WDM) has been gaining steam in the last few decades thanks to developments in laser and accelerator facilities, allowing researchers to better probe these elusive states of matter [1–3]. WDM, though not precisely defined, is generally considered to encompass states with pressures above 100 GPa, temperatures in the range of 1 eV to 100 eV, and high densities, lying at or above solid density [1]. In this regime the plasma displays unique properties, including strongly coupled, fluid-like ions and fully or partially degenerate electrons, which invalidates many standard approximations in the current theory [2] and makes WDM difficult to describe. In addition to this theoretical interest, WDM is of great importance to many fields, ranging from astrophysics, where the study of WDM gives insight into the internal structure and evolution of many celestial objects [4–6], to inertial confinement fusion, relevant for the understanding of implosions of laser fusion capsules [1, 2]. Consequently, many large-scale experiments are conducted on WDM [7–9], which all seek to solve the significant experimental challenges inherent to WDM, i.e. the generation of extreme conditions [2, 4] and the consequently short lifetimes on the order of micro- to nanoseconds [1]. Development of suitable diagnostics for these experiments is therefore essential.

Owing to the high opacity of WDM samples in the optical range, most methods of optical probing are excluded, unless performing surface or shock-wave measurements [1, 2, 10]. In contrast, x-rays are capable of penetrating these samples thanks to longer attenuation lengths, and therefore offer effective diagnostic techniques for probing the bulk properties [7, 11]. Common methods to produce x-rays for WDM experiments include synchrotrons [11], x-ray free electron lasers [12], and laser-driven plasmas. In the latter case, irradiating backlighter targets with high-intensity short-pulse lasers allows generation of high-brightness fast X-ray sources, which can be tuned to desired energy ranges and intensities through the choice of backlighter material and laser energy [7]. The tunability, high intensity, and small angular dependence of the x-ray emission are attractive to WDM matter research, enabling several diagnostic techniques, including x-ray Thomson scattering, phase contrast imaging, radiography, and x-ray absorption spectroscopy [1, 2].

The study of X-ray Absorption Fine-Structure (XAFS), a type of absorption spectroscopy, has a wide range of applications in numerous fields, including biology, solid-state physics [13], and as of 1988 WDM research [14]. In the context of WDM experiments, XAFS often examines the photon energy range around a K-edge, defined by the binding energy of K-shell electrons in a material. By studying the behavior of the absorption spectra in this region for different conditions, multiple properties of WDM, e.g. density, temperature, and coordination of atoms, can be simultaneously extracted [11, 14, 15]. These structures consist of shifts in the location and shape of the K-edge, as well as oscillations in the absorption coefficient after the edge. They originate from free electrons ejected by x-rays through the photoelectric effect. In a simplified description, the wave-functions of these ejected electrons scatter on neighboring atoms, so that a part of the free electron wave-function returns to and interferes with the absorbing atom. As this all occurs in a single

coherent quantum state, the process is effectively a modulation of the quantum electronic state at the location of the absorbing atom. Since the absorption coefficient depends on the available electronic states, this phenomenon causes modulation of the absorption probability, and therefore the absorption spectrum, depending on the atomic order within $\approx 5\text{\AA}$ of the absorbing atom [13].

XAFS can be broken down into two techniques: X-ray Absorption Near Edge Structure (XANES), covering the range of 50 eV within the K-edge [16], and extended x-ray absorption fine-structure (EXAFS), extending as far as 250 eV above the edge [17]. In the case of XANES, the shift and slope of the K-edge are governed by the degeneracy, ionization, and continuum lowering of the plasma and are affected by the temperature and density [2, 18]. For both XANES and EXAFS, the amplitude of the absorption oscillations is an indicator of temperature, while the position and frequency of the peaks reveal information about the density and ionic order [1]. Note that determining properties from the oscillations is more straightforward for EXAFS, as approximations of single scattering are valid in this region, simplifying theoretical models [13]. Due to the fine nature of these structures, good spectral resolution and uniform samples are required [1]. Accordingly, producing homogeneous WDM with sufficiently long lifetimes is key.

The necessity of rapidly depositing large amounts of energy to reach WDM conditions presents a considerable experimental challenge. There are various methods of creating WDM, e.g. diamond anvil cells (DAC) [19], x-ray pulses [9], and high-energy heavy-ion beams [6], among others. Intense heavy-ion beams offer significant advantages in that the penetration range is on the scale of several mm and heating can occur isochorically along the whole sample [1, 20]. As such, producing large WDM samples with relatively long lifetimes and low gradients is possible, opening doors to new WDM physics and easing the diagnostic restrictions. This type of WDM production will be realized at the Facility for Antiproton and Ion Research (FAIR), an accelerator facility under construction in Darmstadt, Germany [10]. Preliminary experiments are underway at a neighboring facility, the GSI Helmholtz Center for Heavy Ion Research [7]. At the High energy, High Temperature (HHT) experimental station and beamline, finished in 2021, high-energy ns-pulse laser beams from the Petawatt High-Energy Laser for Heavy Ion Experiments (PHELIX) are combined with heavy-ion beams originating at the UNiversal Linear ACcelerator (UNILAC) and accelerated by the heavy ion synchrotron SIS-18. Using these heavy-ion beams with velocities of $0.9 c$ [21], ion counts of $\sim 4 \cdot 10^9$ for U^{73+} per FWHM = 100 ns bunch, and an ion focal spot of $\sim 1 \times 1 \text{ mm}^2$ [22], along with PHELIX beams with laser energies of up to 200 J at 2ω (527 nm) for ns-pulses with a FWHW of 25 μm , heavy-ion heating experiments using x-rays from laser-driven plasma can be conducted. As such, GSI offers the, as of writing this, unique ability to combine intense heavy-ion beams with high-energy ns-pulse laser beams [23]. These capabilities will be expanded in the future at the Atomic, Plasma Physics and Applications (APPA) cave at FAIR, in its final stage achieving ion numbers of up to $\sim 5 \cdot 10^{11}$ ions (U^{73+}) per bunch through acceleration in the synchrotron SIS-100 [10]. The APPA cave will combine this more intense heavy-ion beam with a laser system of comparable characteristics to PHELIX, finally reaching the WDM regime with temperature states of up to $> 10 \text{ eV}$ [10].

On the path towards the generation of WDM, an experiment at HHT using the heavy-ions of the SIS-18 synchrotron is planned for 2024, aiming to investigate heavy-ion heated Al samples through absorption spectroscopy of the Al K-edge. The work of this proposal is carried out in the context of a preparatory experiment planned for the summer of 2023, whose goal is to investigate and optimize the x-ray backlighter and XAFS diagnostics setup in a laser-only beamtime using PHELIX. My contribution to this was the design of spectrometers that allow the detection of absorption spectra in the photon energy range of XANES and EXAFS with sufficiently high resolution to resolve the relevant features. As typical for the realm of high-resolution x-ray spectroscopy of extreme-state matter [24], my spectrometers are crystal based. Drawing inspiration from spectrometers successfully implemented in other XAFS experiments [11, 14, 15], I designed and modeled two spectrometers. One is targeted at XANES, uses a double, flat crystal geometry,

and employs ammonium dihydrogen phosphate (ADP) crystals. The other is intended for EXAFS and implements a focusing geometry, known as a Focusing Spectrograph with with Spatial Resolution (FSSR), with a spherically bent mica crystal.

This work is structured as follows. In chapter 2, I explain the fundamentals of x-ray spectrometers, outlining the theory behind them with special focus placed on the FSSR. For the FSSR I collect the sometimes inconsistent information from the literature and reformulate it to present a unified picture. In this chapter I also derive the analytical dispersion of the geometries relevant for this work and elaborate on resolution. In chapter 3, the considerations and constraints placed on the spectrometer design according to their purpose and the experimental setup are listed and explained, followed by the reasoning behind the crystals used in each spectrometer and their geometries in detail. In chapter 4, the calculations and simulations conducted to validate the design and determine the spectral resolution are described, where the results are summarized at the end of the chapter. In chapter 5, I present the mechanical design of the spectrometers and show their 3D-models, along with their alignment procedures. Finally, in the outlook I discuss and summarize the results and describe the goals of the preparatory experiment in 2023 in more detail. Here I want to note that the spectrometer designs, in all their facets, were made possible with the help and input of Artem Martynenko, Zsuzsanna Major, and in particular, Philipp Hesselbach and Paul Neumayer, who contributed the initial designs and offered continued support in all stages of the design process.

2. X-Ray Absorption Fine Spectroscopy

FROM HERE ON THE CHAPTERS ARE COMPLETE EXCEPTING DATA ANALYSIS, RESULTS AND DISCUSSION, AND OUTLOOK. PLEASE NOTE THAT THE FORMATTING AND LAYOUT ISNT DONE YET. I USUALLY ONLY DEAL WITH THAT AT THE VERY VERY END, SINCE STUFF GETS MOVED AROUND ANYWAYS.

As X-ray Absorption Fine Spectroscopy (XAFS), also known as X-ray Absorption Fine-Structure, constitutes the purpose of the spectrometers, this diagnostic technique will be elaborated on first. In essence, this method probes the electronic structure of atoms in a material by irradiating a sample with X-rays and recording the resulting absorption spectrum. It originates from X-ray Absorption Spectroscopy (XAS), a method first theoretically established in 1920 at Lund University. Although XAS was overshadowed by X-ray Diffraction in its first few decades, in large part due to the higher x-ray intensity requirements, it had a key advantage in that it could probe less ordered and liquid materials. As such, the technique experienced a boom in 1975, where the building of large research facilities with electron synchrotrons enabled consistent access to intense x-ray sources. This also marks the advent of XAFS, the modern version of XAS, allowing measurement of the fine structures of absorption edges, which presents the opportunity to locally probe and therefore investigate defects and features in lattice structures to a higher degree than other x-ray diagnostics. With over 50% of beamtime requests from industrial customers for synchrotron laboratories pertaining to x-ray absorption methods, XAFS has become a well-established tool to evaluate samples for a wide array of fields, including Chemistry, Biology and Material Science, among others [25].

XAFS is not only limited to conventional materials. Thanks to x-ray sources capable of short pulses, like laser-produced plasma, as well as detectors with rapid recording, like crystal spectrometers, collection of a complete spectra on the order of nanoseconds is made possible. This in turn enables the study of short time-scale, dynamic phenomenon, including Warm Dense Matter [26], which exists in a non-crystalline state where short-range order dominates, making XAFS especially suited as a diagnostic technique [18]. The first experiment using XAFS on WDM was in 1987, in which converging laser-induced shocks were used to bring an aluminum sample to WDM conditions [14]. Since then, XAFS has been widely used in WDM matter research, with x-ray crystal spectrometers playing a central role [1, 11, 18].

In the context of WDM experiments, XAFS often examines the photon energy range around a K-edge, defined by the binding energy of K-shell electrons in a material. By studying the behavior of the absorption spectra in this region for different conditions, multiple properties of WDM, e.g. density, temperature, and coordination of atoms, can be simultaneously extracted [11, 14, 15]. These structures consist of shifts in the location and shape of the K-edge, as well as oscillations in the absorption coefficient after the edge. They originate from free electrons ejected by x-rays through the photoelectric effect. In a simplified description as depicted in fig 2.1, the wave-functions of these ejected electrons scatter on neighboring atoms, so that a part of the free electron wave-function returns to and interferes with the absorbing atom. As this all occurs in a single coherent quantum state, the process is effectively a modulation of the quantum electronic state at the location of the absorbing atom. Since the absorption coefficient depends on the available electronic



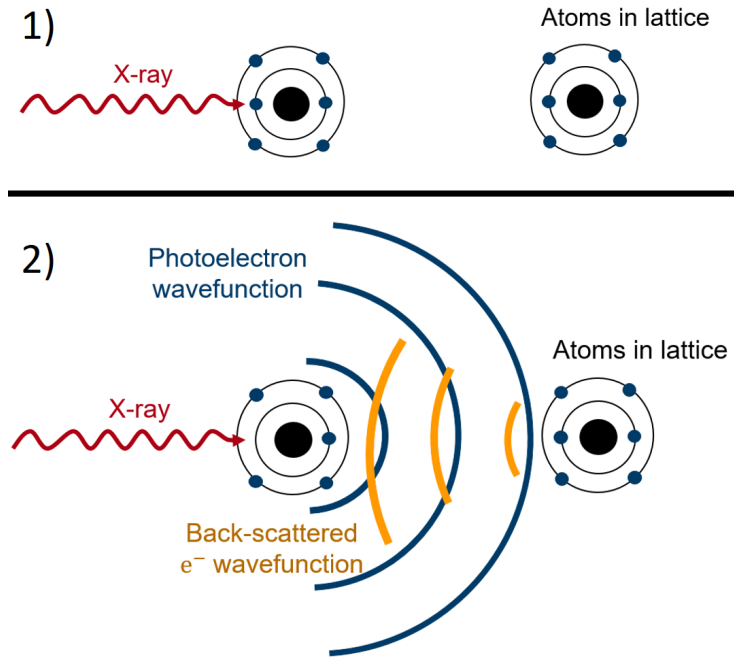


Figure 2.1.: Schematic representation of XAFS mechanism. 1) An electron is ejected from the absorbing atom through the photoelectric effect. 2) The electron wavefunction is partially back scattered by a neighboring atom in a lattice, which returns to the absorbing atom and modulates the electronic states, consequently modulating the absorption coefficient.

states, this phenomenon causes modulation of the absorption probability, and therefore the absorption spectrum, depending on the atomic order within $\approx 5\text{\AA}$ of the absorbing atom [13].

XAFS can be broken down into two techniques: X-ray Absorption Near Edge Structure (XANES), covering the range of 50 eV within the K-edge [16], and extended x-ray absorption fine-structure (EXAFS), extending as far as 250 eV above the edge [17]. In the case of XANES, the shift and slope of the K-edge are governed by the degeneracy, ionization, and continuum lowering of the plasma and are affected by the temperature and density [2, 18]. For both XANES and EXAFS, the amplitude of the absorption oscillations is an indicator of temperature, while the position and frequency of the peaks reveal information about the density and ionic order [1]. Note that determining properties from the oscillations is more straightforward for EXAFS, as approximations of single scattering are valid in this region, simplifying theoretical models [13].

To give an idea of what typical XAFS absorption spectra typically look like and how WDM properties can be determined from them, I will describe two experiments, with one applying XANES and the other EXAFS, whose results are depicted in fig. 2.2. In an experiment conducted by A. Levy *et al* [18] corresponding to fig. 2.2a, WDM of aluminum is produced through isochoric heating with a picosecond proton beam pulse generated by Target Normal Sheath Acceleration (TNSA) on gold targets. The sample is then irradiated with x-rays from a laser-driven plasma backscatterer of erbium, allowing for recording of absorption spectra. By fitting theoretical models and simulations to the experimental near-edge curves, WDM quantities can be extracted, in this case electron temperature and ion-ion correlation. For example, the electron temperature is determined through the variable slope of the K-edge, where a steeper slope indicates a lower temperature. Likewise, the electron temperature can be found by studying the far-edge structures, as shown in fig. 2.2b. In this experiment by R. Torchio *et al* [11], iron samples are compressed and brought to WDM conditions through laser-driven shocks, then diagnosed with x-rays from the beamline ID24, a synchrotron beamline

specialized for x-ray absorption techniques. By using a correlated Debye model, the electron temperature is determined. In addition, information about the atomic structure of the sample is gained by studying the disappearance of certain peaks. Notable is also the broadening of EXAFS oscillations with increasing temperature, which is indicative of a collapse of atomic order in the material.

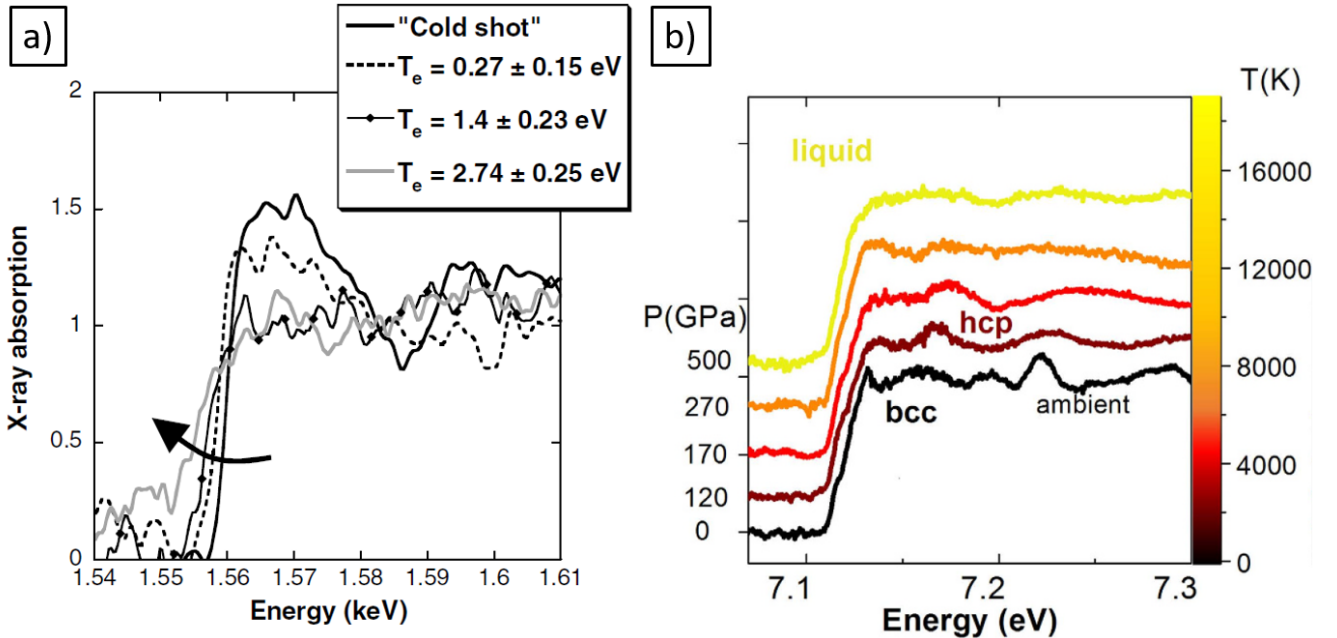


Figure 2.2.: Examples of XAFS spectra taken in WDM experiments for XANES and EXAFS respectively. It is important to note that the first graph displays absorption spectra of aluminum, while the second shows spectra of iron. **a)** Spectra from an aluminum sample isochorically heated to WDM conditions with energetic proton beam and diagnosed with x-rays from laser-driven plasma of erbium. XANES is applied to extract information about the electron temperature and ion-ion correlation [18]. The arrow highlights the reduction of the K-edge slope with rising temperature. **b)** Spectra from an iron sample brought to WDM conditions with a laser-driven shock and investigated with x-rays generated by a synchrotron. EXAFS is conducted to derive the temperature and lattice structure of the samples. Note that the spectra are artificially shifted along the y-axis to represent rising pressure. [11].

Both of these results exemplify the power of XAFS as a diagnostic method for warm dense matter. As with most experiments in this vein, this method is made possible by x-ray spectrometers. Due to a number of restrictions originating from inherent properties of these devices and the volatile nature of WDM experiments, the design of these spectrometers is not trivial. As such, I will go into more depth on their history and design in the following chapter.

3. Fundamentals of X-Ray Spectrometers

Since its inception in 1914 [27], x-ray spectrometers have developed into an indispensable tool for plasma and high-energy density matter research [24]. This can be attributed in part to the unique challenges presented by x-rays and their interaction with matter. Conventional optics cannot be applied, as no absorption free materials are available and sufficient reflectivity is only achieved with grazing-angle incidence, greatly increasing optical aberrations [28]. By necessity, the entire optics of the spectrometers must therefore be realized using as few components as possible. In most cases, this limits the components to three; the x-ray source, the detector, and the dispersive element, which spatially separates the photons according to their energies and in most cases consists of one reflecting surface, as each new surface reduces the intensity of the x-rays on detector. In light of these limitations, x-ray spectrometers are generally designed with the specific experimental scheme and goals in mind and optimized using ray-tracing codes [24].

Central to the function of these spectrometers is the dispersive element. For energies below 250 eV, gratings are generally used, owing to their high reflectivity, while for x-rays from 250 eV -100 keV, and therefore for this work, crystals are more suitable [24]. The spectral dispersion of the x-rays occurs upon reflection on the dispersive element, where optical path differences between incident photons lead to interference. If this difference corresponds to multiples of the photon's wavelength, there is constructive interference, while the reflected intensity of other wavelengths is suppressed. As the optical path difference depends on the incident angle, photons are dispersed according to wavelength. In the case of crystals, this dependence is expressed by Bragg's law [29]

$$n\lambda = 2d_l \sin(\theta), \quad (3.1)$$

where n is the diffraction order, λ the wavelength, d_l the lattice constant, and θ the grazing angle.

In this work I will categorize the wide variety of spectrometer designs into two types; flat crystal and bent crystal. Crystals can be one-dimensionally bent, for example cylindrically, or two-dimensionally, i.e. conanically or spherically. The type and degree of bending is limited by the crystal material and available production methods [28]. Typically, flat crystal spectrometers offer simplicity, ease of build, and more crystal material choice with fewer defects, while bent crystal spectrometers exhibit lower background, more flexible geometries, and potentially high resolution and intensity on detector [24, 28]. As a result, improved signal-to-noise ratios are expected for bent crystal designs, at the cost of more complicated schemes and potential for crystal defects. Also to note is that bent crystals have the potential for imaging.

In this section, I aim to introduce the background and fundamentals needed for this work. First in section 2.1, the flat crystal design is briefly outlined and explained, also serving as a baseline used to introduce some important quantities. In section 2.2, bent crystal designs are discussed, including an overview of the von-Hamos geometry and a more detailed explanation of the Focusing Spectrograph with Spatial Resolution (FSSR) geometry. Then, in section 2.3, the calculations for the dispersion of the spectrometer geometries used in the experiment are shown. Lastly, the influences on the resolution are discussed in section 2.4.

3.1. Flat Crystal Geometries

An example of a flat crystal spectrometer geometry is shown in fig. 3.1, where the Bragg angle of the central energy, corresponding to the ray incident on the center of the detector, is given as θ_0 and a Bragg angle of an arbitrary wavelength as θ . For every incident angle on the crystal, only one wavelength fulfills the Bragg condition, so that the rays are dispersed on the detector with a dispersion $d(E)$, where d gives the location of the rays on the detector. This dispersion equation is essential for processing of the spectra from raw data, and is therefore to be calculated or, for more elaborate geometries, determined using ray-tracing procedures.

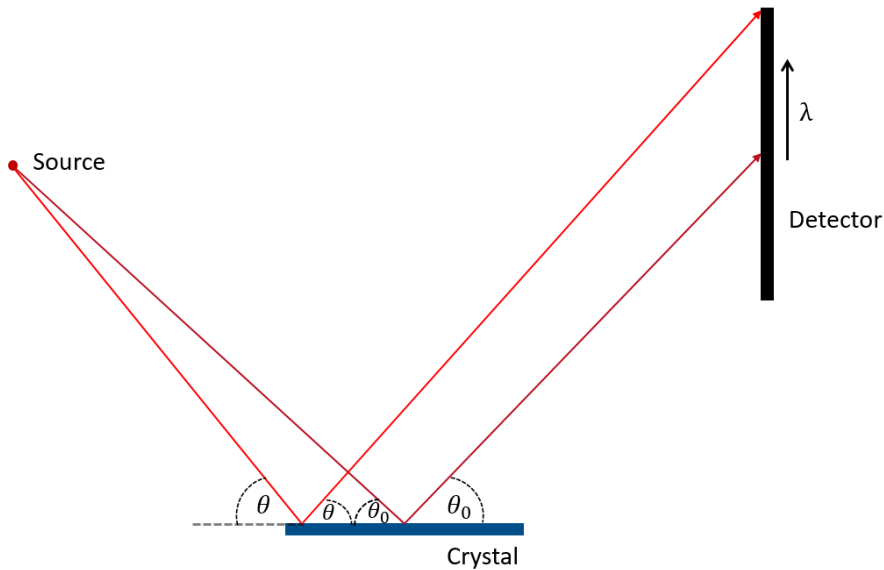


Figure 3.1.: Schematic geometry of a spectrometer with a flat crystal.

Currently, flat crystal spectrometers are typically eschewed in favor of bent crystal in the context of high-energy density matter experiments, attributed to the higher intensity on detector and reduction of source-size influences on the resolution of bent crystal schemes. If flat crystal schemes are used, they often come in as compact, easy-to-use mini-spectrometers, mostly serving supportive roles [24]. Notably, a novel group of flat crystal spectrometers shows promise, employing two vertically orientated plane crystals, but is not suitable for this work due to its lower collection efficiency [30]. Despite this outlook, flat crystal schemes could prove suitable if the experimental scheme covers the drawbacks, i.e. small source size and intense x-ray source, and a simple spectrometer scheme is desired.

3.2. Bent Crystal Geometries

Bending of the crystal allows for higher intensity on the detector, and therefore better signal-to-noise ratios, as the crystals collect the rays more effectively than their flat counterparts. Intuitively, this can be understood as more surface area of the crystal reflecting light of a certain wavelength onto the same approximate region on the detector. This comes at the cost of possibly worsening intrinsic reflection properties of the crystal [31], impacting the inherent resolution due to the crystal, though it is to note

that the focusing properties of the scheme can offset this impact [24]. Spherical crystals often entail FSSR geometries, while cylindrical crystals are applied for von Hamos geometries. Though these are of course not the only possibilities, they are the geometries relevant for this work, and hence will be handled individually in the following.

INTENSITY DISCUSSION THAT VINCENT MENTIONED

3.2.1. Von Hamos

The von Hamos geometry is shown schematically in fig 3.2. In this case the components are placed such that the source and detector lie on the cylinder axis of the crystal. As a result, all rays emitted from a point source with the same incident angle on the crystal are focused onto the same point on the detector, regardless of where they are reflected on the circular arc. In effect, the geometry leads to one dimensional imaging of the source, with the spatial resolution along the y axis and spectral resolution in x direction in fig 3.2. With its high collection efficiency and 1-D imaging, this scheme is popular, but has the drawback of a shallow angle of incidence on the detector and sensitivity to source broadening in the dispersive direction [24].

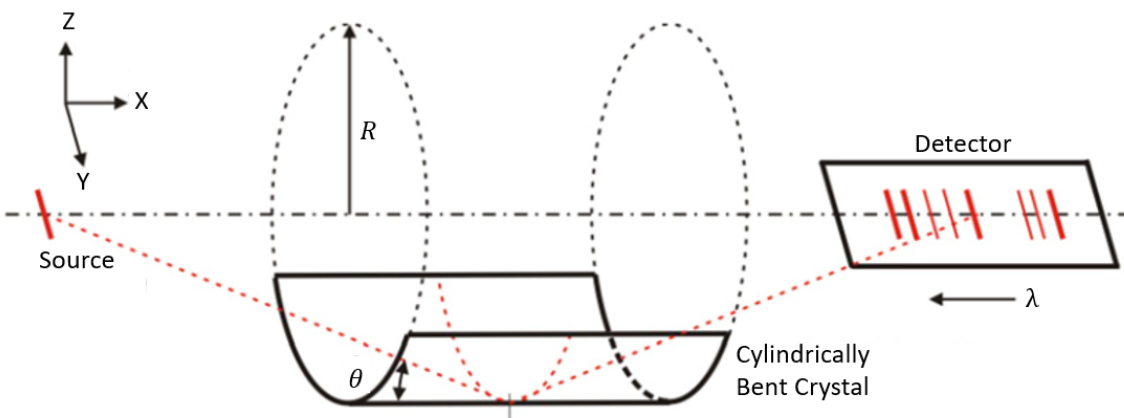
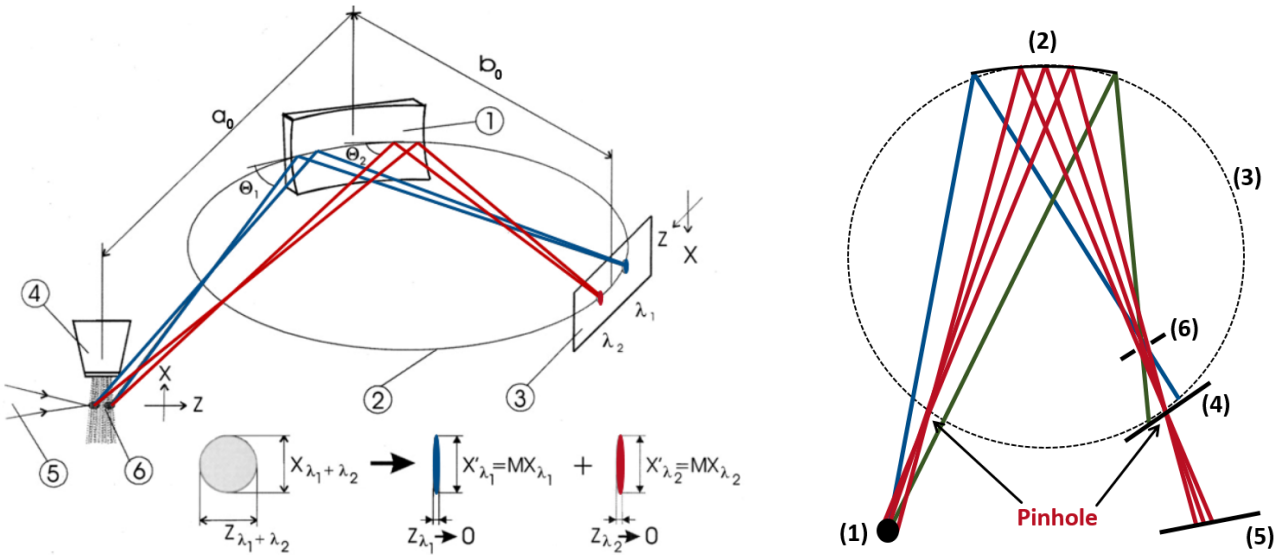


Figure 3.2.: Schematic representation of a spectrometer with von Hamos geometry. R represents the crystal curvature radius. [24]

3.2.2. Focusing Spectrograph with Spatial Resolution

The FSSR has become one of the most widely used spectrometer geometries in plasma diagnostics [29], since it offers high luminosity, spectral and spatial resolution, and relatively large energy ranges [24]. Its geometry is characterized by the use of a spherically bent crystal and is commonly separated into two variants, the FSSR-1D and FSSR-2D, whereby the suffix refers to the dimensions of the source imaging [24, 32]. Due to its comparable simplicity, the function of the FSSR-1D will first be described, followed by the FSSR-2D in the final paragraph.

Before discussing further, I need to make an aside about the terminology used here. When I refer to "imaging", I mean imaging in the sense of rays coming from an object plane being reflected in such a way



(a) Schematic depiction of the FSSR-1D spectrometer. (1) Spherically bent crystal, (2) Rowland circle, (3) detector, (4) target material source (in the diagram a gas, in this work a foil), (5) laser beam, (6) laser-produced plasma. Additionally the imaging of the source is shown on the bottom, where a 1D-image is formed for each wavelength. [32]

(b) Schematic comparison of the FSSR-1D and 2D configurations. (1) Source, (2) spherically bent crystal, (3) Rowland circle, (4) detector in FSSR-1D, (5) detector in FSSR-2D, (6) aperture at polychromatic crossover. Also pictured is the location of the pinhole-like points for the rays of a single wavelength, here in red.

Figure 3.3.: FSSR Schemes.

that an image is formed in the image plane, which depends on from where the rays were emitted. This is analogous to what occurs for lenses and curved mirrors, which is simply the result of refraction or reflection on a curved surface. Furthermore I will differentiate between "mirror imaging" and "pinhole imaging", referring to imaging due to mirror curvature in the first case and pinholes as in pinhole cameras in the second. On the other hand, "spectral focusing" refers to the focusing of the rays of the same wavelength, but from different origins, onto a single point. This is in essence different from imaging, since it does not inherently form an image, although both cases involve a form of focusing.

A schematic representation of the geometry can be found in fig. 3.3a. To explain the workings of the FSSR-1D, it is instructive to define two distinct planes, as the properties of the spectrometer change between them. In this work they are denoted as the dispersive plane, containing the direction of dispersion and the circle depicted in fig 3.3a, and the vertical plane, which is perpendicular to the dispersive plane and includes the detector surface. In the literature these planes are often referred to as the meridional (dispersive) and sagittal (vertical) planes [24, 29]. First, I will focus on the dispersive plane.

An important concept to this configuration in the dispersive plane is Johann geometry [33], which utilizes the so-called Rowland circle (RC) (see fig. 3.3), defined as a circle tangential to the spherical crystal at its midpoint with the radius $R/2$, where R is the radius of the crystal curvature. According to this geometry, any ray with a given wavelength that passes through a certain point on the RC fulfills the Bragg condition everywhere on the crystal surface and is focused in first approximation onto another point on the RC, mirrored across the crystal curvature pole. All other rays of this wavelength, which do not pass through this point, do not fulfill Bragg's law anywhere on the crystal and are hence not reflected. This effectively results in spectral focusing of the light onto the RC independent of where the rays are emitted. This is

schematically illustrated in fig. 3.3a, where the red and blue rays indicate different wavelengths. To note here is also that placing the detector on the RC is the defining feature of the FSSR-1D [34].

For both planes, an additional important aspect is mirror imaging properties originating from the spherical bending, comparable to imaging from a concave mirror and therefore in itself independent of wavelength. There are two focal lengths, one for each plane, which result from astigmatism due to the off-axis location of the source with respect to the crystal. The imaging condition, which follows from the mirror equation, in the vertical plane is [32]

$$\frac{1}{a} + \frac{1}{b} = \frac{(2 \cos(\alpha))}{R}, \quad (3.2)$$

where, for a given ray, the distance between emission point and crystal incidence is denoted as a , the distance between crystal incidence and detector incidence as b and the Bragg angle as θ , with $\alpha = 90^\circ - \theta$. To achieve the best possible spectral resolution, the source-crystal distance a_0 , where the index 0 refers to the central ray, and the crystal-detector distance b_0 are chosen so that eq. 3.2 is satisfied [24, 32, 35]. This ensures sharp imaging in the vertical plane. It is important to note that for the FSSR-1D, there is no imaging on the detector in the dispersive plane, as the detector lies on the point of spectral focusing. Despite this, the mirror imaging in the dispersive plane (see [32]) does lead to a convergence of rays of different wavelengths onto a region between detector and crystal. By placing an aperture on this region, referred to as the polychromatic crossover (see fig. 3.3b), extraneous rays are blocked, reducing the background on the detector [24]. Through mirror imaging and spectral focusing, the FSSR-1D produces a series of 1D, spectrally distinguished images on the detector, as depicted in the bottom of fig. 3.3a.

The other variant is the FSSR-2D, in which case the detector is placed anywhere not on the RC [35]. If the detector and source lie outside of the RC, pinhole imaging for each wavelength is realized in the dispersive plane. The "pinholes" are a result of the spectral focusing and are located on the RC as labeled in fig. 3.3b. A good way to imagine this is by removing everything inside the RC and bringing the "pinholes" together, forming a typical pinhole camera setup for each wavelength. Hence the magnification in the dispersive direction depends on the distance of the source and detector respectively to the RC [24]. This pinhole imaging in the dispersive plane, along with mirror imaging in the vertical plane, results in a series of 2D spectrally selected images on the detector with different magnifications in each plane [36]. In general, the 1D configuration yields the highest possible spectral resolution, since there is minimal overlap of energies due to spectral focusing, while the 2D setup allows for 2D quasi-monochromatic imaging of the source at the cost of reduced spectral resolution [24]. Accordingly, the FSSR-2D setup is suitable for use with a source that emits a quasi-discrete spectrum, as a continuous spectrum would lead to a continuous set of 2D-images, leading to very low spectral resolution.

3.3. Dispersion Calculation

The dispersion $d(E)$ of a spectrometer shows the relation between a spatial coordinate and the energies of the photons. In this work I use d for the coordinate, defined as pictured in fig. 3.4. Therefore $d(E)$ quantifies where each photon with energy E is expected to land on the detector dispersive line for a given spectrometer configuration. Generally speaking, an approximately linear dispersion is desirable, since it simplifies data processing and ensures an even spread of energies on the detector, so that no information is lost due to variable resolution [29]. I will calculate the dispersion for the two geometries used in this work, namely for the flat crystal geometry found in fig. 3.1 and the FSSR as depicted in fig. 3.3b.

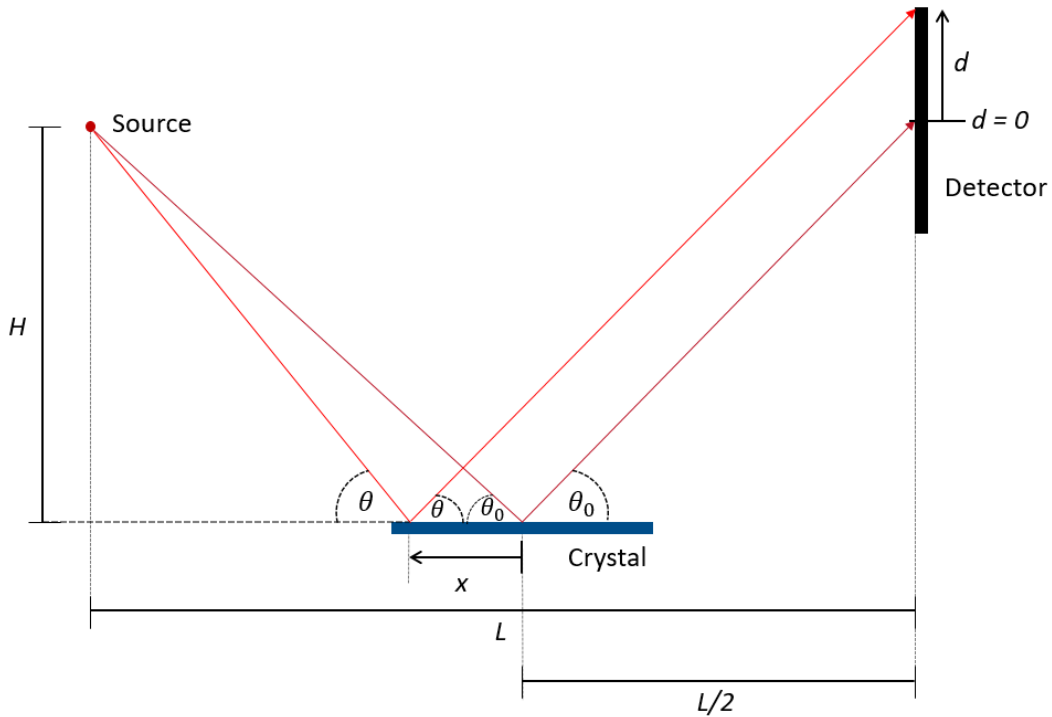


Figure 3.4.: Schematic representation of a flat crystal geometry with the detector perpendicular to the crystal surface. d is defined as lying on the intersection of the dispersive plane and detector surface, with its origin on the location of the central ray, corresponding to θ_0 , on the detector. x is the distance between the incident points of a given ray and of the central ray on the crystal in the dispersive plane. H is the height of the spectrometer, i.e., the vertical distance from the source to the crystal surface, and L is the length of the spectrometer, i.e., the source-detector distance.

I will calculate the dispersion for the flat crystal configuration using trigonometry and the Bragg condition. The parameters used can be referenced from fig. 3.4. From the path of the non-central ray in the diagram with the Bragg angle θ , I get the two relations

$$\tan \theta = \frac{H + d}{\frac{L}{2} + x} \quad (3.3a)$$

$$\tan \theta = \frac{H}{\frac{L}{2} - x}. \quad (3.3b)$$

Setting the right hand sides equal to each other and solving for x yield

$$x = \frac{L}{2} \cdot \frac{d}{d + 2H}. \quad (3.4)$$

I then plug this into eq. 3.3a and simplify, which gives

$$\tan \theta = \frac{d}{L} + \frac{H}{\frac{L}{2}}. \quad (3.5)$$

By identifying $\frac{H}{L/2} = \tan \theta_0$ and solving for d , I can write

$$d = L(\tan \theta - \tan \theta_0). \quad (3.6)$$

Finally, using Bragg's law (see eq. 3.1) and

$$\tan \theta = \frac{\sin \theta}{\sqrt{1 - \sin^2 \theta}} = \frac{1}{\sqrt{1/\sin^2 \theta - 1}}, \quad (3.7)$$

I receive the dispersion for the flat crystal geometry with detector perpendicular to the source

$$d(E) = L \left(\frac{1}{\sqrt{\left(\frac{2d_l}{nhc}\right)^2 E^2 - 1}} - \frac{1}{\sqrt{\left(\frac{2d_l}{nhc}\right)^2 E_0^2 - 1}} \right), \quad (3.8)$$

where E_0 denotes the energy of the central ray, h the Planck constant and c the speed of light, which is used in the conversion $\lambda = hc/E$. Consequently the dispersion is determined by four parameters in total: n , d_l , E_0 and L .

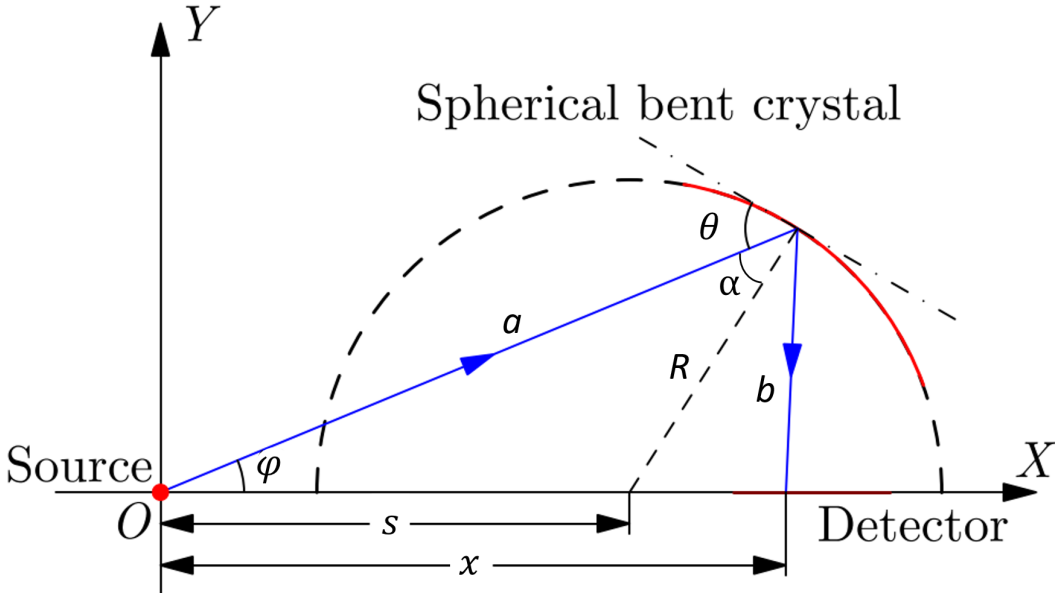


Figure 3.5.: Geometry of an FSSR spectrometer, labeled with quantities useful for analytical calculations. Note that this is generalized, so that it's applicable for both the FSSR-1D and 2D. [29]

Before calculating the FSSR dispersion, it is important to consider a restriction on the detector position. The dispersion line on the detector surface, which corresponds to d , must lie on a symmetry axis of the sphere drawn out from the crystal curvature and point towards the source, so that the imaging condition in the vertical plane (see eq. 3.2) is fulfilled for all photon energies. With this placement, the dispersion can be analytically calculated. Q. Yang *et. al.* [29] carried out this calculation employing the coordinate system and quantities found in fig. 3.5. For the dispersion $x(\varphi(\theta))$ they found

$$x = \frac{2s\chi(\chi + s \cos \varphi)}{\kappa}, \quad (3.9)$$

where

$$\begin{aligned} \chi &= (R^2 - s^2 \sin^2 \varphi)^{1/2} \\ \kappa &= 2\chi^2 + 2s\chi \cos \varphi - R^2. \end{aligned} \quad (3.10)$$

To bring $x(\varphi)$ into the form $d(E)$, I first express χ and κ in terms of α , which is related to the Bragg angle θ through the equation $\alpha = 90^\circ - \theta$. By taking advantage of the triangle traced out by R , a and s , I can write

$$\begin{aligned}\chi &= R \cos(\alpha) \\ \cos \varphi &= \frac{(a - R \cos \alpha)}{s}\end{aligned}\tag{3.11}$$

Plugging this into eq. 3.10 leads to

$$\begin{aligned}\kappa &= 2R^2 \cos^2 \alpha + 2sR \cos \alpha \cos \varphi - R^2 \\ &= 2R^2 \cos^2 \alpha + 2sR \cos \alpha \frac{(a - R \cos \alpha)}{s} - R^2 \\ &= 2Ra \cos \alpha - R^2.\end{aligned}\tag{3.12}$$

From this and $s = \sqrt{a^2 + R^2 - 2aR \cos \alpha}$ follows

$$x(\theta) = \frac{\sqrt{a^2 + R^2 - 2aR \sin \theta}}{1 - \frac{R}{2a \sin \theta}},\tag{3.13}$$

where $\cos \alpha = \sin \theta$ was used. The only implicit dependence on θ left in this equation is in $a(\theta)$. Using the same triangle from above and the fact that s is independent of θ , a can be written as

$$\begin{aligned}a &= R \sin \theta + \sqrt{R^2 \sin^2 \theta + s^2 - R^2} \\ \text{with } s &= \sqrt{a_0^2 + R^2 - 2a_0 R \sin \theta_0},\end{aligned}\tag{3.14}$$

where a_0 and θ_0 denote these values for the central ray. Note that for simplicity a_0 and θ_0 were chosen to calculate s , though any combination of a and θ can be used. To determine $d(E)$, I introduce a coordinate transform according to fig. 3.5 with $x_0 = x(\theta_0)$. In the case of a FSSR-1D geometry, x_0 is equivalent to $a_0 \sin(2\theta_0)$, owing to the right angle of the central ray with the detector surface. Accordingly d can be written as

$$d = x - x_0.\tag{3.15}$$

Applying this transform, Bragg's law as in eq. 3.1 and converting from λ to E as before finally yields

$$d(E) = \frac{\sqrt{a^2 + R^2 - \frac{2Rnhc}{(2d_l)} \cdot \frac{a}{E}}}{1 - \frac{R(2d_l)}{2nhc} \cdot \frac{E}{a}} - x_0,\tag{3.16}$$

where

$$\begin{aligned}a &= \frac{Rnhc}{(2d_l)} \cdot \frac{1}{E} + \sqrt{\left(\frac{Rnhc}{(2d_l)}\right)^2 \cdot \frac{1}{E^2} + s^2 - R^2} \\ \text{with } s &= \sqrt{a_0^2 + R^2 - \frac{2a_0 Rnhc}{(2d_l)} \frac{1}{E_0}}.\end{aligned}\tag{3.17}$$

Therefore, the quantities required to find the dispersion $d(E)$ of an FSSR are the crystal curvature radius R and lattice constant d_l , diffraction order n , central photon energy E_0 , central Bragg angle θ_0 and source-crystal distance a_0 . To note is that this result is applicable for both the FSSR-1D and 2D.

3.4. Resolution

In general, the resolution of a spectrometer mainly depends on three factors [24, 34], which will be discussed in this section:

1. Source broadening
2. Intrinsic crystal properties
3. Detector resolution

Which of these has the greatest effect on the resolution depends on the choice of geometry, crystal and detector.

Source broadening refers to the effect the physical size of the source has on the resolution. For example, in the flat crystal geometry a larger source corresponds to a larger area covered by x-rays of the same wavelength on the detector, leading to worse resolution. This factor is strongly dependent on the geometry and crystal shape. Generally, the resolution of flat crystal spectrometers is strongly affected by source broadening, while FSSR spectrometers suppress the influence of source size [24].

The crystal properties that mainly affect resolution are structural in nature. The crystal structure influence is parameterized by the rocking curve width $\Delta\theta$, which is given by the FWHM of the reflected intensity as a function of incident angle and depends on wavelength and polarization of the radiation, crystal perfectness and bending radius [24, 31]. The reflection properties, mainly affecting the intensity on detector, are assessed using the integrated reflectivity R_{int} , i.e., the ratio of the angular intensity $I(\theta)$ integrated over the range of diffraction angles around a Bragg angle $\theta_B \pm \Delta\theta$ and the incident intensity I_0 [31]

$$R_{int} = \frac{1}{I_0} \int_{\theta_B - \Delta\theta}^{\theta_B + \Delta\theta} I d\theta. \quad (3.18)$$

Both these quantities can be calculated using the dynamical theory of X-ray diffraction [31]. In this work the following formula will be used to estimate the ratio of integrated reflectivity for a given setup,

$$R_{int} = \frac{N_{det}}{N_{total}} \frac{4\pi D}{\Delta x_{pix}}, \quad (3.19)$$

where N_{total} represents the total number of photons emitted by the source in the energy range, often corresponding to an emission line, D the distance over which the x-rays diverge (for example, the optical path length from source to detector for flat crystal geometries), and Δx_{pix} the pixel width in dispersive direction. N_{det} corresponds to the number of photons detected over the same energy range as N_{total} , corrected for filter transmission and detector sensitivity [37]. Note that a high resolution usually implies a low R_{int} and therefore weaker signals on the detector. With these quantities the effect of the crystal on the resolution can be estimated.

Another factor for the spectrometer resolution is the detector spatial resolution. This can be estimated simply by using the dispersion $d(E)$ and spatial resolution dx of the detector. In this work this takes the form of pixel density on a CCD camera. This is often the limiting factor for FSSR spectrometers [24, 34], though this should be calculated on a case to case basis, as geometry design choices also impact this factor.

For geometries capable of imaging, one can differentiate between spatial and spectral resolution. The spectral resolution is given directly by the energy interval corresponding to the area covered on the detector

by X-rays of the same wavelength, while the spatial resolution results from the imaged source size on the detector and is only limited by deviation from the imaging condition for different locations on the X-ray source.

In the case of the von Hamos geometry, the spectral resolution is sensitive to source broadening in both x and z directions, as depicted in fig. 3.2, while the spatial resolution along the y axis remains unaffected [24]. For the FSSR-1D, the spectral resolution is independent of source size due to the spectral focusing in the dispersive plane, a property that applies for the spatial resolution in the vertical plane as well, owing to the large a distance relative to the typical source size in laser plasma experiments. In the FSSR-2D scheme, the optimal spectral focusing condition is no longer met, therefore a finite source size leads to source broadening in spectral direction as well. [34]. A geometrical calculation of the impact of source size on spectral resolution for the FSSR scheme can be found in [38].

4. Spectrometer Design

As stated in the introduction, the overarching goal is the eventual characterization of warm dense matter of aluminum. The WDM will be induced using a heavy-ion beam, leading to rapid and fairly homogeneous heating compared to other techniques, like laser-driven shock or proton beams. Since WDM is opaque to visible light, x-rays will be used for the main diagnostics. In this case, the source will be laser-driven plasma as a backlighter of the sample, distinguished by its tunability, high-brightness, and small angular dependence of the emission. Together, the laser-driven backlighter and heavy-ion beam heated WDM sample offer a relatively homogeneous setup, in reference to sample properties and x-ray spatial distribution. This homogeneity enhances the diagnostics in that approximately a single WDM state can be probed, reducing unknowns in the experiment. XAFS will be the diagnostic method of choice, a technique that notably enables measurements relating to the atomic structure of short-lived, non-crystalline matter. As previously outlined, x-ray spectrometers are ubiquitous in WDM experiments using XAFS, and here is no exception.

The design of the spectrometers must in essence accommodate each main aspect of the experiment. The heavy-ion heating places demands on the sample size to ensure homogeneity and induces large amounts of background, necessitating careful shielding. The laser-driven backscatterers impact the possible intensity and wavelength distribution of the x-ray source, such that the spectrometers must be adjusted accordingly. Finally, the use of XAFS sets restrictions on the photon energy range of the spectra and the resolution, as the features must be detected and resolved. The details of all these design considerations will be discussed shortly in the next section.

In this chapter I will discuss the designs of the spectrometers and their rationale, outlining the advantages and disadvantages of each. First, I will describe the considerations that informed the designs. Then, the geometries of each spectrometer will be introduced in detail. Finally, the specifications of the spectrometers will be given and a comparison carried out, summarizing the purpose of each design.

4.1. Design Considerations

For the design of the spectrometers I took five main considerations into account, which follow from the specific needs of the experimental setup:

1. **Energy Range:** As stated in the introduction, the main function of the spectrometers is to perform X-ray Absorption Fine Structure (XAFS) spectroscopy and resolve the aluminum K-edge at 1558.98 eV [39] and its features. Near edge structures (XANES) can be observed within 50 eV of the edge [16], while extended fine structures (EXAFS) can be measured as far as 250 eV above the Al K-edge [17], which consist mainly of several oscillations in the absorption coefficient [15]. This yields an energy range of approximately 1530 - 1810 eV, where the upper value is much less strict than the

lower and the lower value is adjusted upward if the spectral range of the spectrometer is mainly the immediate area of the K-edge.

2. **Sample Size:** The future heavy ion beam heating, although more homogeneous than other WDM production methods, still is partly inhomogeneous, since the energy deposited along the heavy ion beam propagation direction, denoted here as z , is not constant. This negatively impacts the absorption spectroscopy, and accordingly the sample temperature measurements through XAFS, as each transmission location on the sample along the z direction corresponds to a certain energy on the detector (see fig. 4.1). The setup must therefore be adjusted to heat the sample as homogeneously as possible, realized by carefully choosing the sample-source distance and sample size in z direction. This limit on sample size also introduces a restriction on the choice of central Bragg angle. Together, this leads to the following constraints: (1) the central Bragg angle cannot be too large, because, assuming a fixed energy range, a larger θ_0 requires a larger range of angles to cover all the energies compared to a smaller θ_0 . This is due to the proportionality $\lambda \propto \sin \theta$, in which larger wavelengths have smaller slopes. (2) The source-sample distance cannot be too small, as then the heavy ion beam would strike the laser target, nor too large, as that would require a larger sample size. The sample size is limited by the projection of the spectrometer angle range on the sample, as well as by the FWHM of the heavy ion beam transversal to z . A compromise between all these factors leads to a sample-source distance of 5 mm and a sample size in z direction of ≤ 1 mm. Fig. 4.1 illustrates the setup and gives the distances used in this work.
3. **Spectral Resolution:** The main requirement on the spectral resolution is that it be high enough to resolve XAFS structures. From the example spectrum given in fig. 2.2a, the required resolutions for XANES can be estimated. Practically, a spectral resolution of ≤ 1 eV is expected to resolve the Al K-edge sufficiently to carry out XANES, while ~ 10 eV is required for EXAFS, estimated from half of an oscillation period [15]. Spatial resolution is advantageous, but not a hard requirement.
4. **Intensity:** A high enough intensity to resolve the spectra and perform the absorption spectroscopy is necessary. In the design this comes into play in part through the length of the spectrometer and distance to the source. Additionally the choice of geometry and crystal play a role.
5. **Physical Size:** The spectrometers must fit in the HHT chamber. This restricts the physical length to under 0.55 m. There must also be space for the heavy ion beam in future experiments and the PHELIX beam.

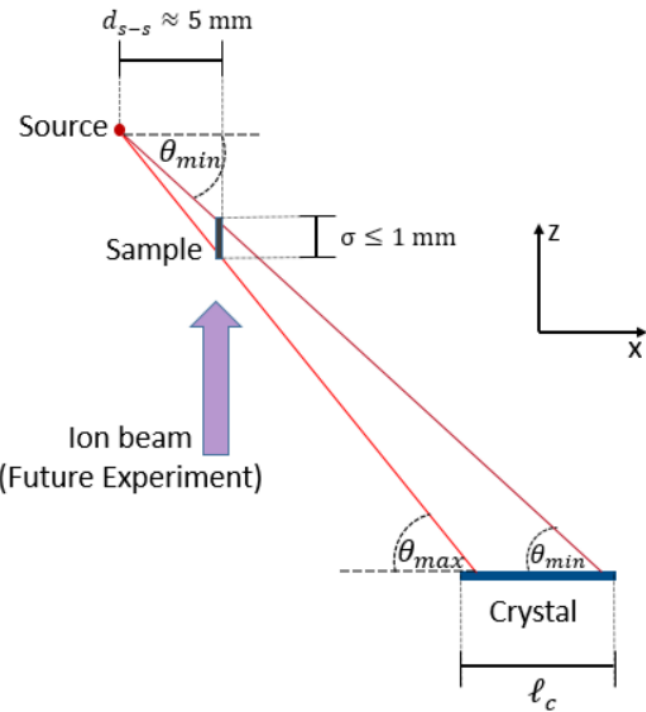


Figure 4.1: Illustration of the sample size consideration. The transmission length on the sample in z direction is denoted by σ , which must stay at or below 1 mm. θ_{max} and θ_{min} correspond to the maximum and minimum Bragg angles of the spectrometer respectively, while ℓ_c represents the length of the crystal in the dispersive plane and d_{s-s} the source-sample distance.

4.2. Implemented Spectrometer Schemes

I chose two configurations according to the considerations above and the aspects discussed in the introduction to this chapter, namely a flat crystal geometry (see fig. 3.1) and a bent crystal scheme, specifically a FSSR-1D geometry (see fig. 3.3). For the flat crystal spectrometer, inspiration was drawn from [15] and a dual channel geometry was chosen, so that both the absorption and source spectrum could be simultaneously measured on a single detector. A flat crystal design has potential in light of the small source size in the form of a laser-driven plasma ($\approx 150 \mu\text{m}$) and possibility of intense emission thanks to the source's tunability. This helps to alleviate the inherent disadvantages of a flat crystal geometry outlined in section 3.1.

As for the bent crystal scheme, the FSSR-1D geometry offers the highest possible spectral resolution of FSSR schemes while also giving high luminosity on detector. Additionally, it has the potential for 1D imaging in the vertical direction, which could be exploited to simultaneously observe the source and absorption spectra. I also considered a FSSR-2D configuration, but decided against it because some source spectra are expected to be continuous, which would significantly impact the spectral resolution. A von Hamos geometry was discarded because of its aforementioned shallow incidence angle on the detector and sensitivity to source broadening, which is altogether absent in the FSSR-1D scheme.

The crystals for each scheme were chosen according to the considerations listed in the appendix (section I). In the end, I decided on using ammonium dihydrogen phosphate (ADP) for the flat crystal geometry

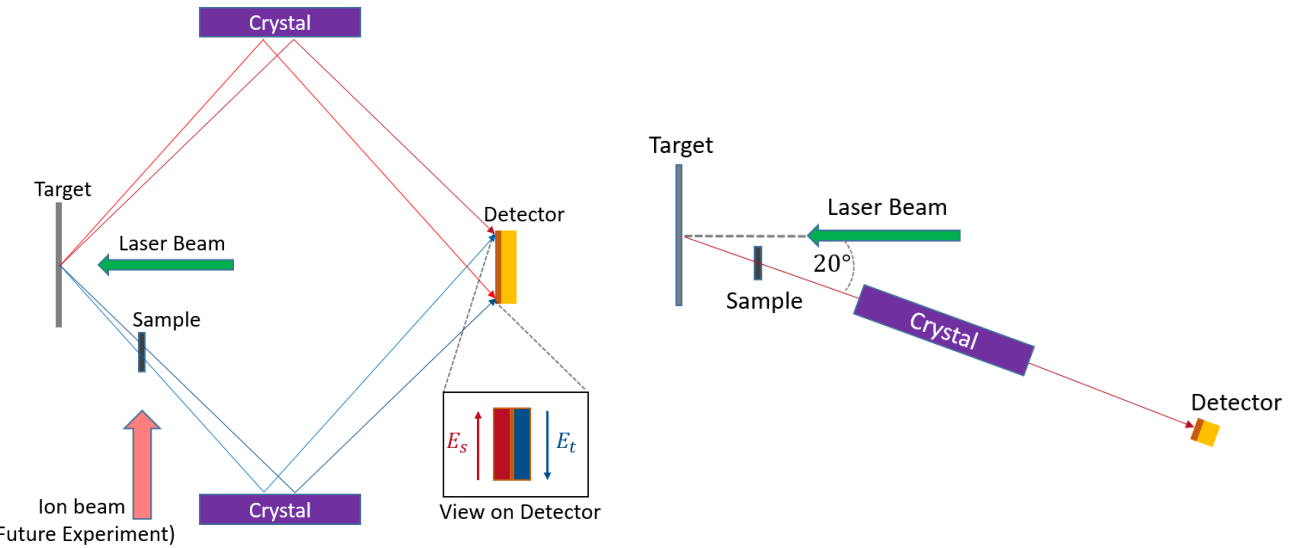
and mica for the bent crystal. ADP was chosen mainly for its potential to reach extremely high optical and structural perfection as well as its lattice spacing of $2d_l = 10.64 \text{ \AA}$, allowing for diffraction in the first order, covering the desired energy range [40, 41]. Mica was chosen for the FSSR-1D geometry for its bendability, high spectral resolution in tandem with good reflectivity, a wealth of previous applications in the literature and the possibility to use a low diffraction order (second order), yielding $2d_l/n = 19.84/2 \text{ \AA} = 9.92 \text{ \AA}$. [24, 32, 34, 35]. One drawback of the mica crystal was that it contains aluminum, which could lead to a drop in reflectivity at the Al K-edge, though the expected decrease in intensity is not significant enough to exclude mica [42]. Mica is also often used in FSSR spectrometers with strong bending, reaching radii of down to 100 mm [34].

In addition to the two main spectrometers of this work, I will introduce another simple flat crystal spectrometer in section 4.2.3, whose purpose is to deliver a wide energy range overview spectrum of the x-ray source as a control. It uses a potassium acid phthalate (KAP) crystal. This crystal is commonly used in x-ray spectrometers and has a larger rocking curve width than ADP [28, 43]. As this spectrometer is straightforward and not of my design, I will only describe it briefly and give its specifications.

In the following, I will describe the spectrometers in more detail, leaving the specifications for the next section. To note is that for this work I will generally refer to the spectrometers by their geometries, whose basic layout is in principle independent of the chosen crystal and energy range. For ease of discussion, I will however make clear in the following subsections if I'm referring to the geometry or the spectrometer. After this, the geometry names will refer to the spectrometers as a whole.

4.2.1. Dual Unbent Crystal Spectrometer

The dual crystal spectrometer geometry, which I christened the **Dual Unbent Crystal SpeCtrometer (DUCC)**, is illustrated schematically in fig. 4.2. The central idea behind this geometry is to simultaneously record two spectra by implementing a mirror symmetrical two-channel design. This spatial symmetry ensures that the channels see the same source, assuming a conical symmetry of the plasma emission. Through the combination of the DUCC geometry and ADP crystal, the DUCC spectrometer will target XANES and therefore have a relatively small energy range. This allows for lower relative resolutions, further reducing the impact of source broadening.



(a) Top view including the ion beam, which will not yet be introduced in the experiment. The coverage of rays on the detector according to the origin is depicted above. E_s refers to the source spectrum, while E_t labels the transmission spectrum, corresponding to the bottom beam paths in fig. 4.2a. The red area on the detector shows the E_s coverage and the blue area the E_t coverage.

(b) Side view, in which the tilt of the spectrometer is illustrated.

Figure 4.2.: Schematic illustration of the DUCC geometry, not to scale.

In fig. 4.2a the top view of the DUCC geometry is schematically shown. The laser beam irradiates the target, igniting a plasma. This plasma then emits soft x-rays, whose spectrum is measured through the top channel using one half of the available detector surface. The transmission spectrum through the sample, in this work an aluminum foil, is recorded through the bottom channel on the other half of the chip surface. The separation of the two spectra on the chip is realized by a plate with two openings inserted into the beam path before the two channels overlap (not shown in fig). Space was left for the ion beam for future experiments, which is of course not present in this work. To note is that space is left in the center of the spectrometer for a large lead block, which in the future will serve to shield the detector from electrons and protons being emitted from the sample due to the interaction with the heavy ion beam. Fig. 4.2b depicts the 20° tilt of the DUCC spectrometer that I introduced to leave space for the laser beam, which is conical and has a half opening angle of $\pm 2.3^\circ$. The spectrometer components were also tilted to simplify the design and deliver the simplest possible profile on the detector.

4.2.2. Focusing Spectrograph with Spatial Resolution

The FSSR-1D configuration used for the spectrometer is depicted in fig. 4.3. As the fundamental geometry effectively functions equivalently to the one described in section 3.2.2, I will not elaborate in detail on it here and instead discuss the spectrometer as a whole, so a FSSR-1D geometry with mica crystal. The main focus of this spectrometer is to capture a larger energy range, aiming to additionally resolve the oscillations in the EXAFS in the absorption spectra, while maintaining a good spectral resolution. Furthermore, the larger source-crystal distance a_0 and relation with the crystal-detector distance b_0 (see eq. 3.2) allow freedom of placement in the chamber, as compared to the DUCC spectrometer. One potential drawback

is the necessity of careful alignment and exact positioning of the components to achieve high spectral resolution, owing to the innate focusing and imaging of the FSSR scheme.

To note is that the potential of the 1D imaging for absorption spectroscopy with a single detector is not applied here due to the ratio of a_0 to b_0 , leading to a magnification in the vertical plane of 0.22. This magnification combined with the small sample size σ renders an image too small to consistently differentiate between source and transmission spectra. Despite this, the imaging properties does find use in concentrating the x-rays from the plasma onto a single line in the dispersive direction on the detector, significantly reducing the effects of background, which will be especially advantageous in the future experiments with the heavy ion beam.

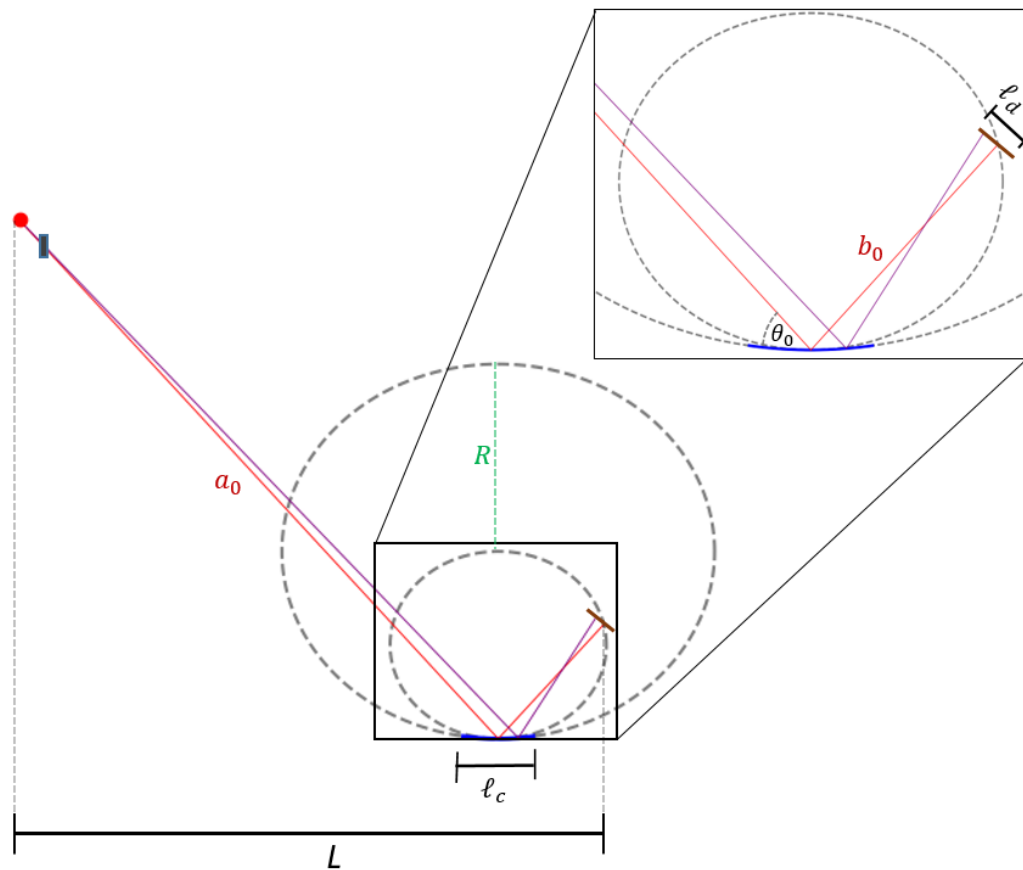


Figure 4.3.: Schematic Illustration of the FSSR-1D, where R is the radius of curvature of the crystal, L the spectrometer length, ℓ_c the length of the crystal in the dispersive plane and ℓ_d the detector length in dispersive direction. The crystal is depicted in blue, the source in red and the sample in dark gray. Note that the Rowland circle and circle drawn out by the crystal curvature are also shown.

4.2.3. Single Unbent Crystal Spectrometer

The **Single Unbent Crystal SpeCtrometer** (SUCC) is a basic spectrometer, consisting of a single, flat crystal set in a geometry analogous to fig. 3.1 or to the top channel of the DUCC geometry (see fig. 4.2a). Designed by P. Hesselbach, the spectrometer aims at a large enough energy range to cover both the FSSR-1D and DUCC spectrometer ranges, albeit at a lower resolution, owing to the source broadening intrinsic to the

flat crystal geometry and the worse crystal properties of KAP as compared to ADP. To note is that this higher rocking curve width also increases the intensity on the detector, ensuring that control spectra are consistently recorded. Its role as a control implies that it will not be used for transmission spectra.

4.3. Specifications and Comparison

Now that the specific geometries and crystal choices are established, I will introduce the specifications of each spectrometer and use them to validate that the considerations are fulfilled, as well as compare the spectrometers. The parameters are listed in table 4.1. In the table, the first six parameters are directly relevant to the considerations presented in section 4.1, where all but the spectral resolution follow directly from geometrical calculations. The spectral resolutions are derived using simulations conducted with the python3 code *mmpxrt* from Michal Šmíd [44]. For details on these simulations and path to the final resolution values, see section II in the appendix. In summary, the resolutions are calculated from three contributions: source broadening, detector resolution, and broadening from crystal properties. For the DUCC, the greatest contribution is due to source broadening, while for the FSSR-1D the crystal properties have by far the greatest impact. Additionally, the dispersion for each spectrometer is determined from the simulations, and for the FSSR-1D with a simple ray-tracing code written by me, and compared to the analytical dispersions from section 3.3. For both spectrometers, the analytical and simulated dispersions show excellent agreement and are approximately linear, with the three different derivations for the FSSR-1D dispersion displaying near perfect overlap.

The DUCC with ADP crystals aims to resolve a narrow energy range around the Al K-edge as well as possible to conduct XANES. Consequently, this design successfully fulfills the energy range consideration. The sample size in z direction σ is calculated using the geometry in fig. 4.1, as well as assuming a source size in z direction s_z of 150 μm , which yields the equation

$$\sigma = (\tan \theta_{max} - \tan \theta_{min}) \cdot d_{s-s} + s_z, \quad (4.1)$$

where d_{s-s} corresponds to the source-sample distance and θ_{max} and θ_{min} to the maximum and minimum Bragg angle of the spectrometer. This equation, along with the values in table 4.1, result in a σ well below the upper limit of 1 mm, which together with the chosen θ_0 and d_{s-s} fulfill the sample size consideration. The spectral resolution falls in the desired range of ≤ 1 eV. The small distances from source to detector address the intensity consideration, while a spectrometer length of ≤ 550 mm complies with the physical size consideration.

Next, the validity of the FSSR-1D with mica crystal design will be assessed. With a maximum energy of 1755 eV, the spectrometer is within the range to conduct EXAFS, fulfilling the energy range consideration. As previously, σ , θ_0 and d_{s-s} all fall within the goal, with σ being only slightly larger than 1 mm, where in this case the sample size is determined using the 3D-model of the FSSR-1D in the HHT chamber, as the angle of the sample w.r.t. the crystal depends on the placement of the FSSR-1D in the experimental setup. Accordingly, the sample size consideration is also achieved. With an energy resolution of 3.097 eV, which is well under the requirement for EXAFS of 10 eV, the spectrometer fulfills the spectral resolution consideration as well. The intensity consideration is addressed by the properties of the FSSR geometry and the good intrinsic properties of mica [31, 34]. As with the DUCC, the FSSR-1D also fits well in the experimental chamber. Accordingly, all of the considerations outlined in the beginning of this chapter are fulfilled for both spectrometers.

I will now collect the arguments for each spectrometer interspersed throughout this chapter and present a comparison. Essentially for the purposes of this work, the question is whether to use a flat or bent crystal geometry, which depends also on the experimental conditions. The DUCC offers simplicity of design, easy alignment, and better crystal properties, at the cost of low collection efficiency and high sensitivity to source broadening. Conversely, the FSSR-1D boasts high collection efficiency, effective background reduction, and independence to source size, but is significantly more complex, difficult to align, and vulnerable to crystal defects caused by bending. As seen in table 4.1, for both spectrometers the relative resolution, i.e. $\Delta E/(E_{max} - E_{min})$, is approximately the same at $\approx 1\%$. The sample size σ and central Bragg angle θ_0 are also comparable. This implies that neither spectrometer distinguishes itself solely in terms of its specifications, besides the fact that the DUCC is intended for XANES and the FSSR-1D for EXAFS. In conclusion, the more advantageous design will be determined largely qualitatively from its performance in the preparatory experiment, assuming that the derived numbers prove accurate.

Lastly, I will address the SUCC and its role in this work. As is apparent from table 4.1, the SUCC covers a wider energy range than even the FSSR and therefore is intended for source characterization and acting as a control for the spectra of the DUCC and FSSR-1D. Another important aspect of this spectrometer is the chosen crystal, the KAP. This crystal has an approximately two times larger integrated reflectivity than the ADP (≈ 80 and $33 \mu\text{rad}$ respectively [45]), meaning that the SUCC's inherent resolution due to crystal properties is lower than the DUCC's, while simultaneously contributing to a higher intensity on detector. Consequently, a good signal to noise ratio is to be expected for most potential sources, further cementing its role as a control. Finally, this spectrometer design has been tested and vetted in previous experiments. As such, the SUCC can act as an effective backup, should either the DUCC or FSSR-1D have difficulties in the course of the experiment.

Table 4.1.: Parameters of the DUCC with ADP crystals, FSSR-1D with mica crystal, and SUCC with KAP crystal. All spectrometers use a CCD camera as a detector. The parameters directly significant to the design considerations are listed first, followed by values that set the final geometry but are not immediately relevant to the considerations. The spectral resolution is calculated using the results from section iv, summarized in table II.1. Source size is assumed to be 150 μm . Sample size σ is determined using eq. 4.1 for the DUCC and directly from the 3-D model for the FSSR-1D.

Parameter	Denoted as	DUCC	FSSR-1D	SUCC
Energy Range	-	1541 - 1618 eV	1465 - 1755 eV	1400 - 1800 eV
Sample size (z)	σ	0.75 mm	1.07 mm	-
Source-Sample Distance	d_{s-s}	5 mm	5 mm	-
Central Bragg Angle	θ_0	47.58°	51.36°	17.23°
Spectral Resolution	ΔE	0.703 eV	3.097 eV	-
Spectrometer Length	L	235.17 mm	404.3 mm	325.22 mm
Bragg Angle Range	-	46.01 - 49.14°	45.4 - 58.53°	14.99 - 19.42°
Source-crystal Distance	a_0	174.10 mm	549.71 mm	170.26 mm
Crystal-detector Distance	b_0	174.10 mm	121.11 mm	170.26 mm
Detector Length	ℓ_d	27.6 mm	27.6 mm	27.6 mm
Detector Width	-	6.9 mm	6.9 mm	6.9 mm
Crystal Length	ℓ_c	40 mm	50 mm	50 mm
Crystal Width	-	30 mm	10 mm	20 mm
Crystal Radius	R	-	155.04 mm	-

5. Experimental Setup

Now that the spectrometer designs and important background information are established, I will describe the experimental setup for the laser-only experiment of May 2023 at the High energy, High Temperature experimental station (HHT) of GSI. To reiterate, this experiment is conducted to prepare for a combined experiment, so using PHELIX and the SIS-18 heavy ion synchrotron, in 2024, which is in itself a preparation for eventual combined experiments at the currently in construction FAIR facility, specifically at the APPA cave. This future endeavor will be capable of producing WDM samples through heavy-ion beam heating using the SIS-100, applying the novel combination of laser-driven plasma as backscatterers and heavy-ion heated WDM. The basic experimental scheme is illustrated in the introduction in fig. **REFERENCE WHEN IS CREATED.**

The main goals of the 2023 experiment are to assess the performance of the spectrometers, test backscatterer materials, and to validate the setup as a whole. As the main focus of this work are the spectrometers, I will only schematically explain the general experimental setup in the first section, placing more of a focus on the mechanical design of the spectrometers themselves, which appear in the following section.

5.1. General Setup

The experimental setup, as shown schematically in fig. 5.1 and as an *Inventor* model in fig. 5.2, consists of five main components: the backscatterer target, aluminum sample, spectrometers, PHELIX beam, and focus diagnostics. To note is that the location of heavy-ion beam is also taken into account by the setup. Laser shots that use an aluminum sample are denoted as transmission shots, while reference shots without samples are called source shots. Additionally, a measurement event, initiated by a shot from the PHELIX laser, is referred to simply as an event. From each event results one set of spectra. In the following, I will describe each component individually as well as discuss how the measurements are generally conducted.

The backscatterer targets are irradiated with the PHELIX laser to form plasmas as x-ray sources for the sample diagnostics. To find an optimal backscatterer for future experiments, a variety of materials are tested, including the rare earths samarium (Sm), gadolinium (Gd), terbium (Tb) and dysprosium (Dy), along with polytetrafluoroethylene (PTFE), also known by the brand name teflon. In addition, and most relevant to this work, aluminum (Al) targets are shot, fulfilling the purpose of characterizing the spectrometers and validating the setup using a well-described emission source. All of the targets are rectangular foils with a variety of thicknesses: 100 μm for the rare earths, 120 μm for teflon and 20 μm or 50 μm for aluminum. The targets are affixed to holders placed on a target ladder and aligned to the target chamber center (TCC) for each event. These holders also position the aluminum samples at the aforementioned 5 mm away from the backscatterers.

These samples are penetrated by the x-rays, which are transmitted to the spectrometers. The location of the samples is such that they lie in the optical path of the FSSR-1D and the bottom channel (w.r.t fig. 5.1) of

the DUCC. Most of the samples have a thickness of 0.8 mm, with the exception of the first five transmission shots, which are 2 mm. The switch to 0.8 mm occurred due to the low intensity of the transmission spectra with the thicker samples. The samples remain unheated for the duration of the experiment, so that all transmission spectra are intended to be at ambient temperatures.

The spectrometers lie next on the path of the x-rays, whose mechanical design, with the exception of the SUCC, is discussed in the next sections in more detail. As seen in fig. 5.1, the layout is such that during a transmission shot, so with a sample, the FSSR-1D and bottom channel of the DUCC can record transmission spectra, while the SUCC and upper channel of the DUCC take the reference, or source, spectra. Due to the limitation of only having two x-ray cameras, the spectrometers are designed to be modular, with the cameras easily detachable. Generally speaking, one of these cameras is attached to the SUCC, yielding wide energy range reference spectra, while the other is on either the DUCC or FSSR-1D. Between shots, filters were often changed to accommodate different backscatter intensities, which depend on laser energy and backscatter material. In total, four filter materials were used: carbon, gold, pokalon, and polycarbonate. For each shot, a combination of filter types and thicknesses were chosen according to the backscatter and spectrometer. All the spectrometers are orientated so that they view the backscatter at the same radial angle, exploiting the assumed conical symmetry of the plasma emissions. As such, the SUCC is tilted upwards and positioned above the upper DUCC channel, along with the view of the FSSR-1D placed slightly above the lower channel of the DUCC. Consequently, only the FSSR-1D lies in the plane drawn by the PHELIX beam, backscatter, and sample.

The PHELIX beam is focused onto the backscatter targets with ... **FILL IN SPECS HERE**. The focus diagnostics consist of an optical setup designed to image the TCC onto a camera that lies outside the vacuum chamber. It is used to align the targets and PHELIX beam to ensure clean shots. The chamber is evacuated to establish a vacuum and the x-ray cameras are cooled to near 0°C before each shot to protect the chips from condensation.

After event number 25 (of 75 total events), a phase plate was inserted into the PHELIX beam. With this, a random, spatially distributed phase was introduced, leading to a larger focus spot with a more homogeneous intensity distribution as compared to a Gaussian. Thus the fluctuation between shots was reduced and the homogeneity of the plasma improved.

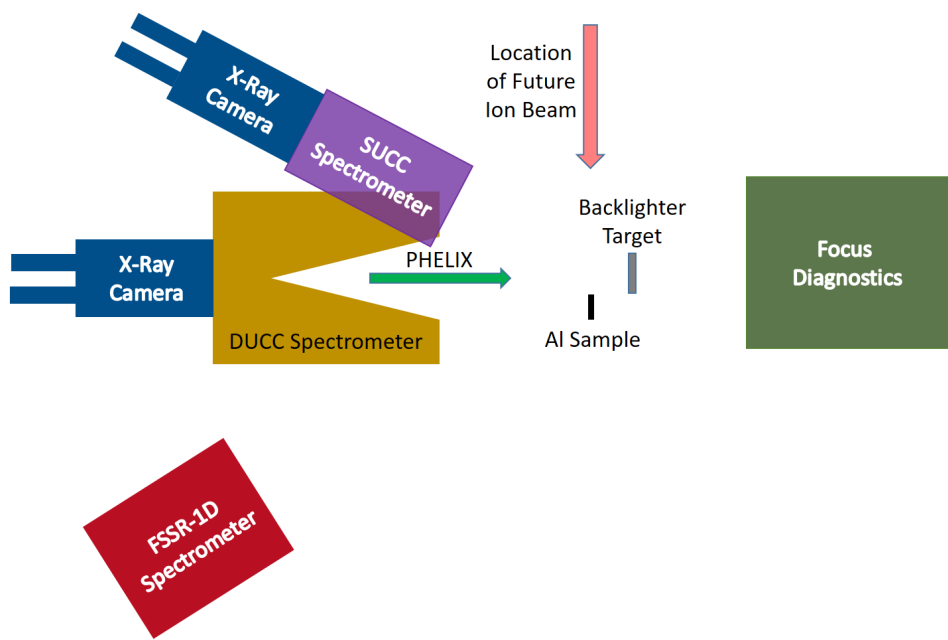


Figure 5.1.: Schematic illustration of the experimental setup. Note that the location of the heavy-ion beam for future experiments is marked, but of course not present in this experiment. The DUCC and SUCC spectrometers are not in the plane of the illustration, but tilted downwards and upwards respectively. The x-ray cameras can be freely transferred between the spectrometers.

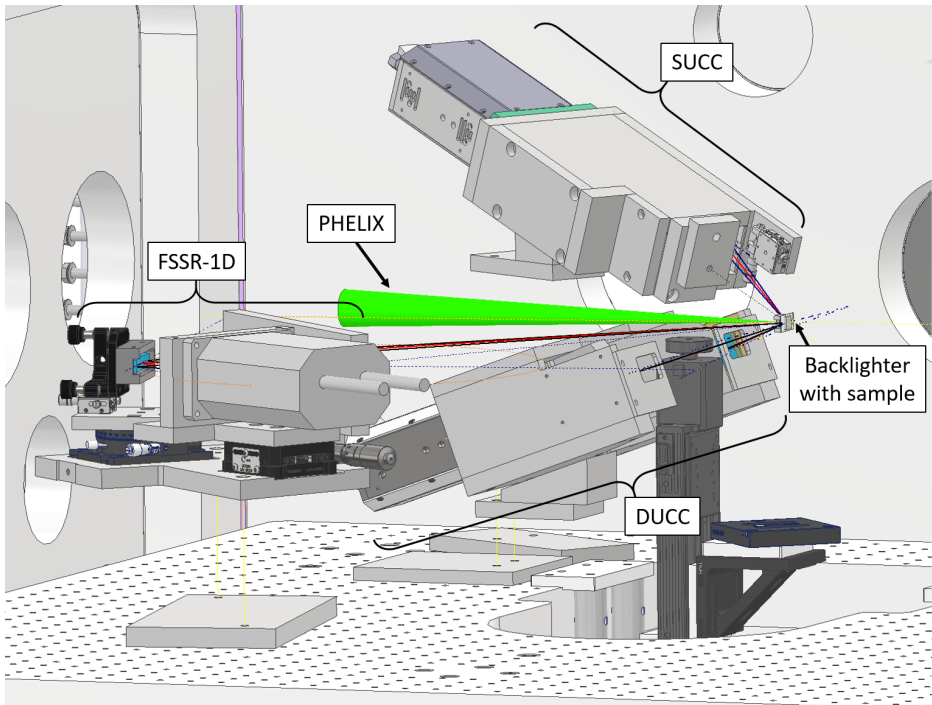


Figure 5.2.: *Inventor* model of the HHT chamber from the perspective of the bottom right of fig. 5.1 looking towards the spectrometers. The heavy-ion beam as well as the focus diagnostics are not pictured. The optical posts that connect the spectrometers to their bases are not shown, but their locations are depicted with thin yellow lines. Additionally, the optical paths in the dispersive direction for each spectrometer are shown in blue, with a red line for the central rays. In actuality the PHelix beam extends out of the chamber.

5.2. Mechanical Design of Spectrometers

ADD REAL PICTURES OF SPECTROMETERS

I based the mechanical design of the spectrometers around four goals. First, the devices must implement the designs presented in chapter 4 to an approximately ± 0.5 mm precision, ensuring that sufficient internal and external alignment to produce well-resolved spectra is achieved. Second, the crystal and camera chip must be sufficiently shielded while still maintaining enough intensity on the detector. Third, alignment of the spectrometer components to one another and the backlighter must be addressed. This requirement is more stringent for the FSSR-1D as a consequence of its focusing properties. Finally, the devices must be robust enough to withstand the harsh experimental conditions resulting from the heavy-ion beam and plasma. This mainly takes the form of heavy aluminum shielding, among others.

In this section, I will describe the mechanical designs of the DUCC and FSSR-1D, whose models are built in the CAD program *Autodesk Inventor 2020*. The SUCC will not be elaborated on, as it is not designed by me and generally shares a similar mechanical design philosophy with a single channel of the DUCC. All spectrometers are outfitted with in-vacuum CCD cameras from *greateyes* of the GE-VAC 2048 512 series as detectors. In the case of the DUCC, an adjusted camera with a thinner front plate is used to avoid clipping. The spectrometer parts are generally made of aluminum, unless otherwise specified.

5.2.1. Dual Unbent Crystal Spectrometer

The DUCC model is shown in fig. 5.3 with the parts color coded, which is presented in table 5.1, along with a summary of their functions and names. The most numerous parts are the ones responsible for shielding and structure. These protect the chip and crystals from debris, particles and extraneous rays. Also serving a shielding role is a pointer holder, whose main purpose is to hold the optical post for alignment purposes.

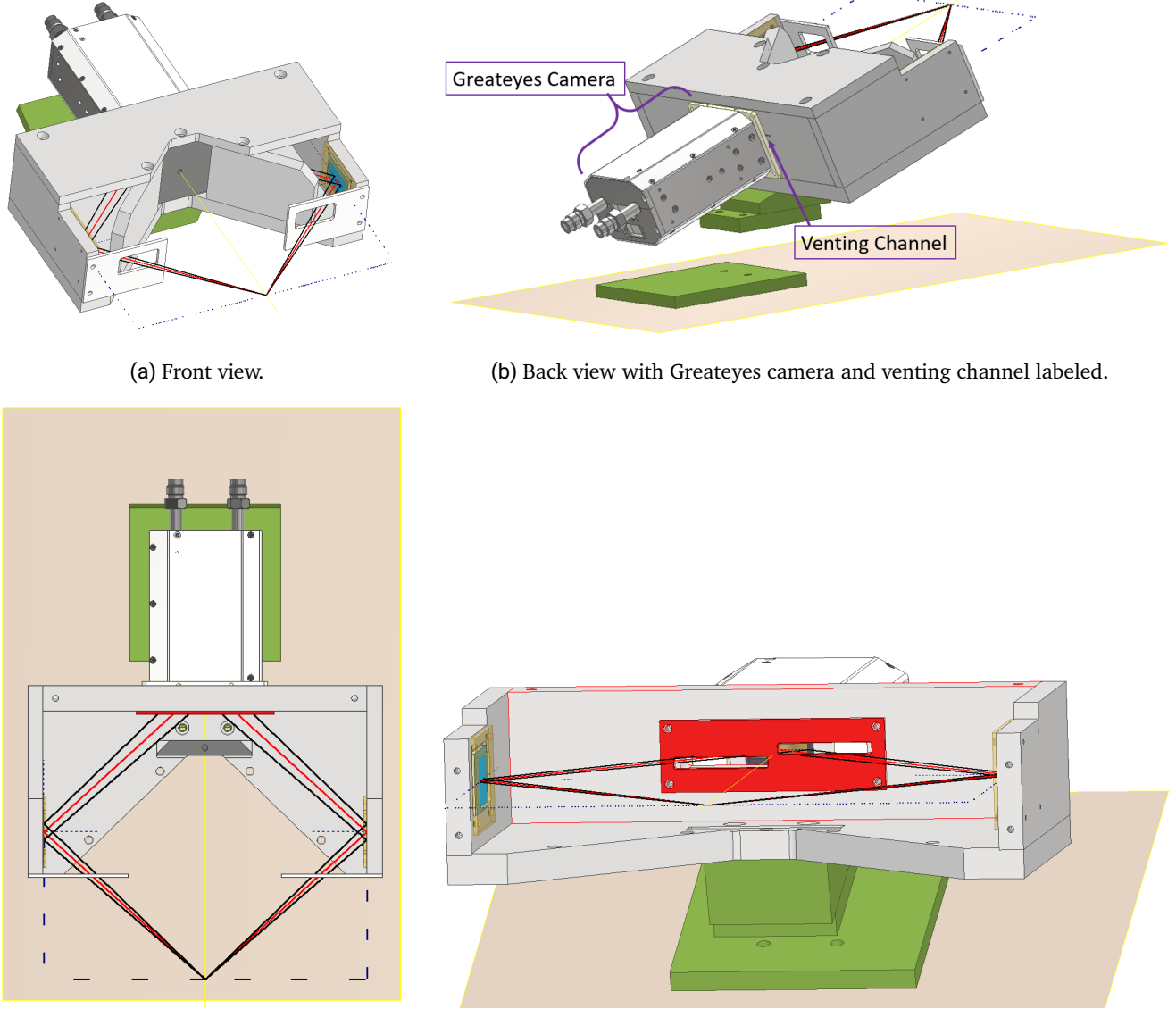
The blast shields, on which $2\text{ }\mu\text{m}$ Mylar foils are attached to the opening, protect the crystal from debris while allowing the x-rays through. Additionally, two carbon filters are glued onto the openings of the filter holder, which are light-tight and prevent visible light from reaching the chip. These carbon filters can be chosen to have an areal density of $\approx 200\text{ }\mu\text{g}/\text{cm}^2$ or $\approx 900\text{ }\mu\text{g}/\text{cm}^2$, depending on the intensities observed on the chips in the experiment. The filter holder also serves to spatially separate the two channels onto the chip, where the holes have a vertical separation of 1 mm so that a shadow will appear on the center line of the chip.

The ADP crystals are held in place by first placing them in a groove, then screwing on the crystal frames made of Trovidur. By attaching a plexiglass foil to the bottom of the groove and fabricating the frames out of plastic, the crystal is protected from direct contact with the aluminum housing. The 20° angle of the DUCC w.r.t. the PHELIX beam is implemented by an angled block of the foot. Finally, a venting channel is engraved into the plate attached to the camera, partially visible in fig. 5.3b. This channel is designed with random turns, similar to a snake, so that air can escape while light is kept out. This is essential to prevent the carbon filters from breaking during venting of the HHT chamber.

The alignment is realized by first affixing the pointer holder with screws to the top and bottom plates of the shielding, making sure to use the groove on the bottom plate to guarantee proper orientation. Then an optical post is set to the designed distance from the front surface of the pointer holder to the x-ray source. The post is attached to the pointer holder and the DUCC is brought into the chamber. Once the tip of the post is as close as possible to the laser-target interaction point, known as the target chamber center (TCC), the spectrometer is aligned, as the alignment of further degrees of freedom is guaranteed by the mechanical precision of the structural pieces, reaching the desired precision of $\pm 0.5\text{ mm}$.

Table 5.1.: Color code of the DUCC model with the functions and name of the parts.

Color	Function	Name
Light gray	Structural/Shielding	-
White (near source)	Protecting crystal	Blast shield
White (labeled)	Capturing spectra	Greateyes camera
Brown	Capturing spectra	Camera chip
Dark gray	Holding alignment post	Pointer holder
Red (front of camera)	Separating spectra/holding filter	Filter holder
Transparent yellow	Securing crystals	Crystal frame
Turquoise	Dispersion of rays	ADP crystal
Green	Supporting + tilting spectrometer	Foot with angled block
Beige	Display location of chamber floor	Breadboard floor
Red	-	Central ray
Black	-	Outer rays



(c) Top view with top and inner shielding hidden. (d) Front view with top and inner shielding as well as the pointer holder hidden.

Figure 5.3.: CAD model of the DUCC. The parts are color coded, whose function and name are listed in table 5.1. The optical posts between the foot parts are not depicted.

5.2.2. Focusing Spectrograph with Spatial Resolution

In fig. 5.4 the FSSR-1D model is pictured with the parts color coded, presented in table 5.2 with a summary of their functions and names. The shielding in this setup is mainly taken care of by the front plate closest to TCC. A snout, formed by three plates, adds additional shielding in front of the chip, as well as functioning as an aperture at the polychromatic crossover as described in section 3.2.2. Inside the snout is the carbon filter holder, which fulfills the same role as with the DUCC, except this time using only the $\approx 900 \mu\text{g}/\text{cm}^2$ carbon filter. Additionally, a blast shield is attached to the front plate, set up the same way as in the DUCC. The crystal itself was originally planned to be fixed by the crystal holder, designed in such a way that the

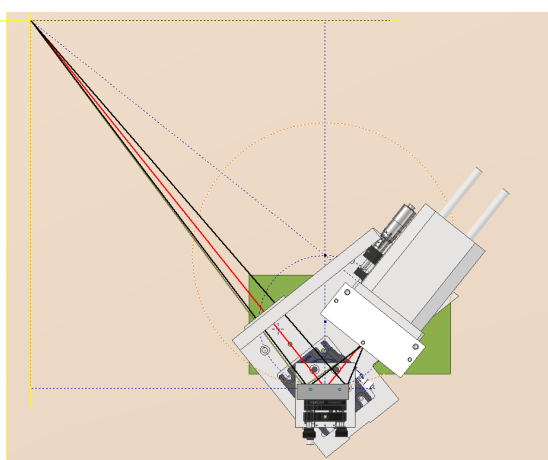
reflecting surface does not come into contact with anything. In the experiment, this holder couldn't be used, as the mica crystal was a different one than planned, namely one that came in its own holder.

Shown in fig. 5.4 are also optical stages utilized for the alignment procedure, which must be more exacting than that of the DUCC, owing to the curvature of the crystal and therefore the imaging and focusing properties. As the alignment is an involved process using additional components not pictured in fig. 5.4, it is described in detail in the appendix, section III.

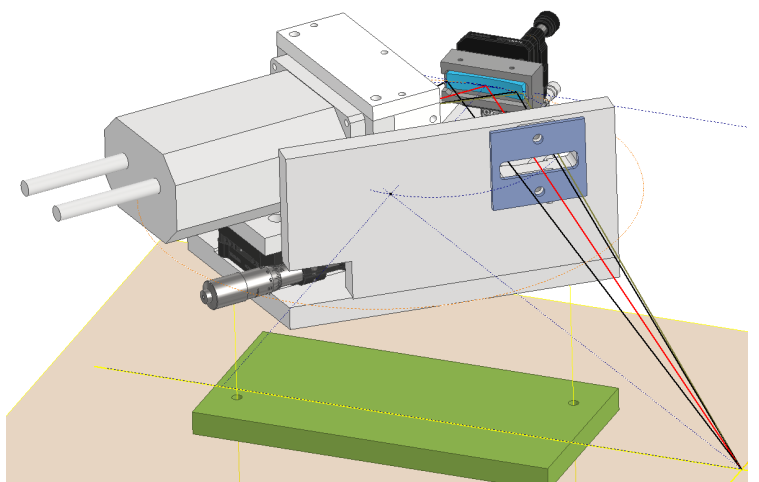
The precision of the internal alignment of ± 0.5 mm is realized with a series of grooves, where each part attached to the main plate is set into a groove. The alignment process use the various optical stages further guarantees the desired precision.

Table 5.2.: Color code of the FSSR-1D model with the functions and name of the parts. Note that there are four optical stages which are not color coded. These are used in the alignment process, so are labeled in fig. III.1.

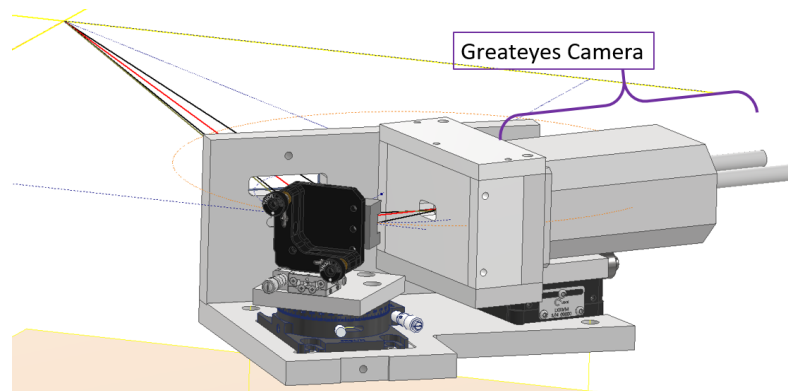
Color	Function	Name
Light gray	Structural/Shielding	-
Light gray (labeled)	Capturing spectra	Greateyes camera
Brown	Capturing spectra	Camera chip
White	Aperture at crossover/Shielding	Snout
Dark gray	Securing crystal	Crystal holder
Red (front of camera)	Holding carbon filter	Filter holder
Dark blue	Protecting crystal	Blast shield
Turquoise	Dispersion of rays	Mica crystal
Green	Support	Foot
Beige	Display location of chamber floor	Breadboard floor
Red	-	Central ray
Black	-	Outer rays
Olive green	-	Highest energy ray



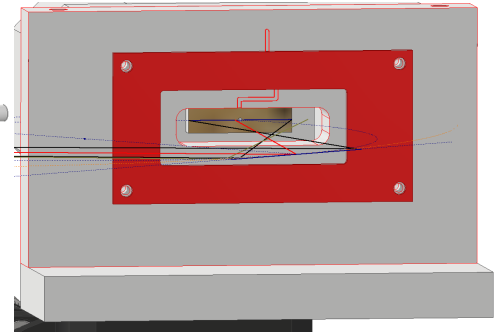
(a) Top view.



(b) Front view.



(c) Back view with Greateyes camera labeled.



(d) View onto chip with snout and camera apparatus hidden. Venting channel is shown behind the filter holder.

Figure 5.4.: CAD model of the FSSR-1D. The parts are color coded, whose function and name are listed in table 5.2. Note that the optical posts between foot and bottom plate are not shown. The various optical stages for aligning the spectrometer are shown, but not color coded.

6. Data Analysis

With the experimental setup established, I will now move onto the data analysis. The goal of this analysis is in general the characterization of the spectrometers and assessment of their performance. For clarity, the analyses will fall into three categories:

1. **Qualitative Performance:** In this section, the fundamental outputs of the spectrometer will be presented, which take the form of source spectra of various backlighter targets as well as absorption spectra of cold aluminum, where here cold refers to ambient vacuum temperatures. This serves to give a picture of how each spectrometer performs and to touch on the properties of the laser-driven backlights.
2. **Spectrometer Characterization:** This category covers the focus of this work, in that the spectrometers properties will be quantitatively assessed. The spectral resolution will be determined through two spectrum features: the He- α (corresponding to the $n=2$ to $n=1$ transition of He-like ions, starting from $2p^1P_1$) line of aluminum from source spectra and the Al K-edge in transmission spectra. Additionally, the ratio of integrated reflectivities of both spectrometers for a given event will be calculated. The integrated reflectivity itself can not be directly determined, as the total emission of the x-ray sources are unknown. Together, these quantities give an idea of how the spectrometers stack up to the theoretical expectations.
3. **Setup Validation:** The purpose of this section is to check that the experimental setup behaves as expected, in the sense that it yields reasonable spectra, which can be validated against predictions from experience and the literature. Two quantities are investigated: the conversion efficiency of the laser energy into an Al He- α emission line and the ratio of the He- α and Lyman-alpha (Ly- α) ($n=2$ to $n=1$ transition of a Hydrogen-like ion, starting from $2p_{3/2}$) lines of aluminum. With these, the aluminum spectra can be qualitatively validated.

I carry out all these analyses with a program that I developed in *python3*, which is capable of taking a raw spectrum in the form of a TIFF image and outputting a fully processed spectrum, as well as performing any of the data analyses outlined in this chapter. The code is designed from the ground up to be applicable to any spectrometer and allow "online" data analysis during a beamtime, producing results for any given event in less than a few minutes. It is my hope that this code lets future researchers involved in WDM research through XAFS at PHELIX effectively interpret and act on raw data in a beamtime, simplifying the workflow.

This code consists of two main parts. The first is responsible for producing workable spectra from raw TIFF images, while the second encompasses any further data analysis, including corrections not directly related to the raw images. The general workflow of the code to produce an emission spectrum is illustrated in fig. 6.1. First, horizontal line outs of each spectrum in the TIFF image are taken by selecting the corresponding area in the image and averaging over the pixels in the vertical direction. This yields the counts for each pixel, which are numbered starting from the leftmost edge of the image. Next, spectra are flipped depending on the orientation of the camera chip and spectrometer channels. The background spectrum is subtracted and

the pixel number is converted to photon energy according to the dispersion of the spectrometer. To note is that this dispersion must be first calibrated by a previous known emission line, in this work the Al He α line. At this point the second part of the code, the data analysis, takes over. To get the emission spectra, the filters are first corrected out using the transmission values from the CXRO database of Berkeley Lab. Then, the camera influences are addressed with the formula

$$N_{ph,det} = \frac{N_{counts} \cdot E_{hole}}{G \cdot E_{ph} \cdot Qe},$$

where $N_{ph,det}$ corresponds to the number of photons incident on a pixel for a given energy and N_{counts} is the counts of the original spectrum. The gain (G), energy needed to generate a photoelectron (E_{hole}), and quantum efficiency (Qe) are all properties of the x-ray camera found in its specification sheet. Finally, the data is smoothed through binning, resulting in the number of photons on detector over the photon energy.

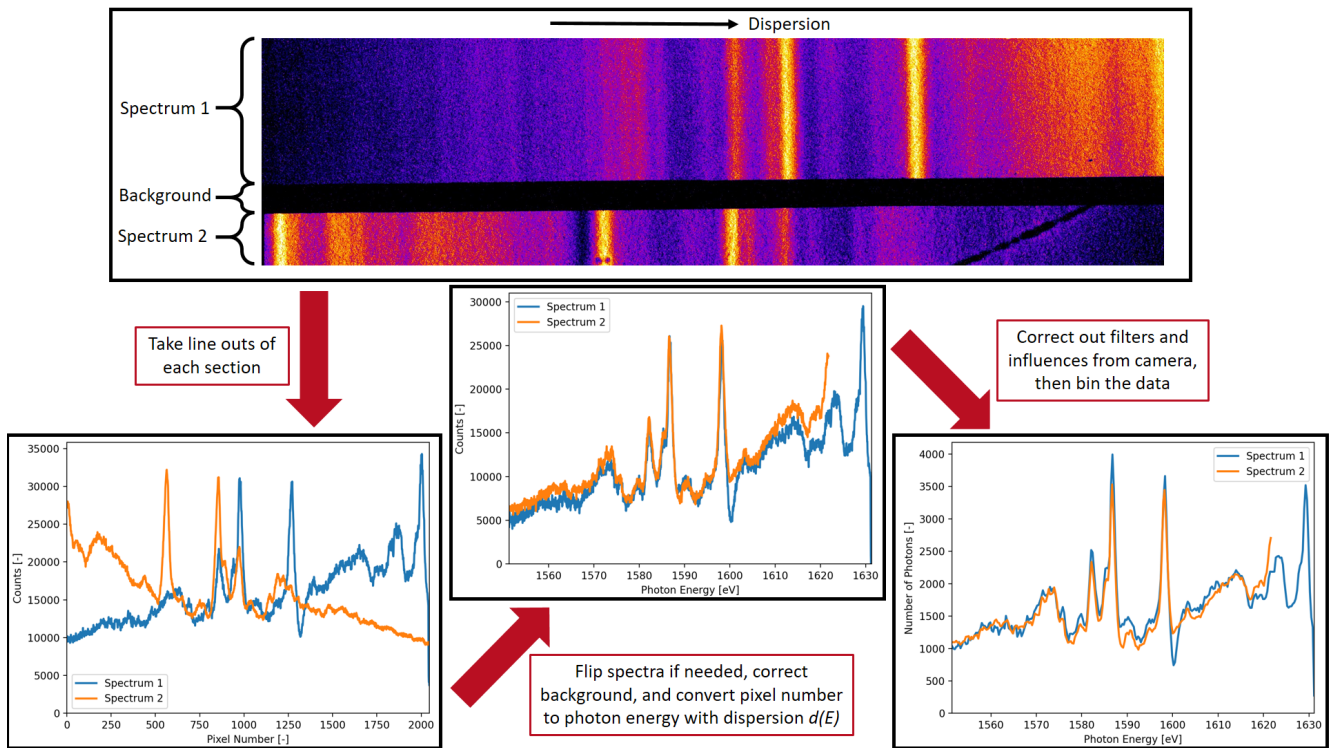


Figure 6.1.: Overview of the data analysis steps from raw TIFF image to fully processed spectrum. Example is of spectra from a Dy plasma ignited with a 57.3 J laser pulse, recorded with the DUCC. In the raw image, the higher the count, the warmer the color, so yellow represents the maxima and dark purple towards black the minima.

In this chapter, I will begin with the qualitative performance, which will be prefaced by a brief introduction to the main types of emission of plasma, since it is important for the discussion of the source and absorption spectra. This will be followed by the spectrometer characterization, containing the spectral resolution and integrated reflectivity ratios of each spectrometer. Finally, I will present the setup validation, which will check the Al plasma spectra against known values from the literature.

6.1. Qualitative Performance

From here on in this section I only present the results without much explanation. Sorry about that, I got significantly delayed during the data processing by some unexpected results. The results given here are as optimal as I can get the data processing and pull from the best shots and data. I'll most likely only be able to continue consistently with writing in November, but if you have any questions regarding the processing in the meantime don't hesitate to ask.

The code in its current form is on github under the url https://git.gsi.de/al_exafs/laser-only-wdm/-/tree/main/Codes. I will warn that the data processing library has become a bit chaotic due to my rushing. It should mostly still work as intended, but still tread with caution.

6.1.1. X-ray Emission Spectra

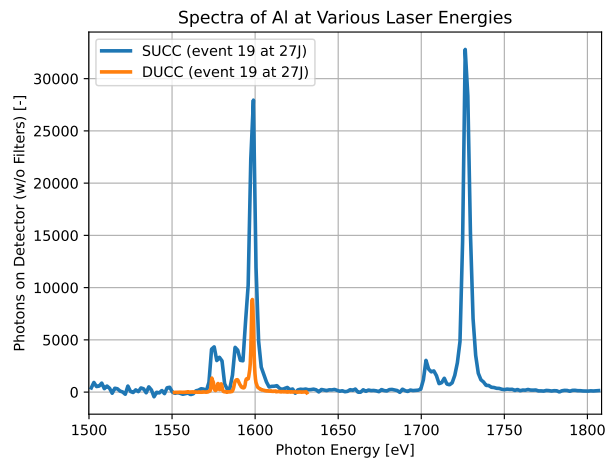


Figure 6.2.

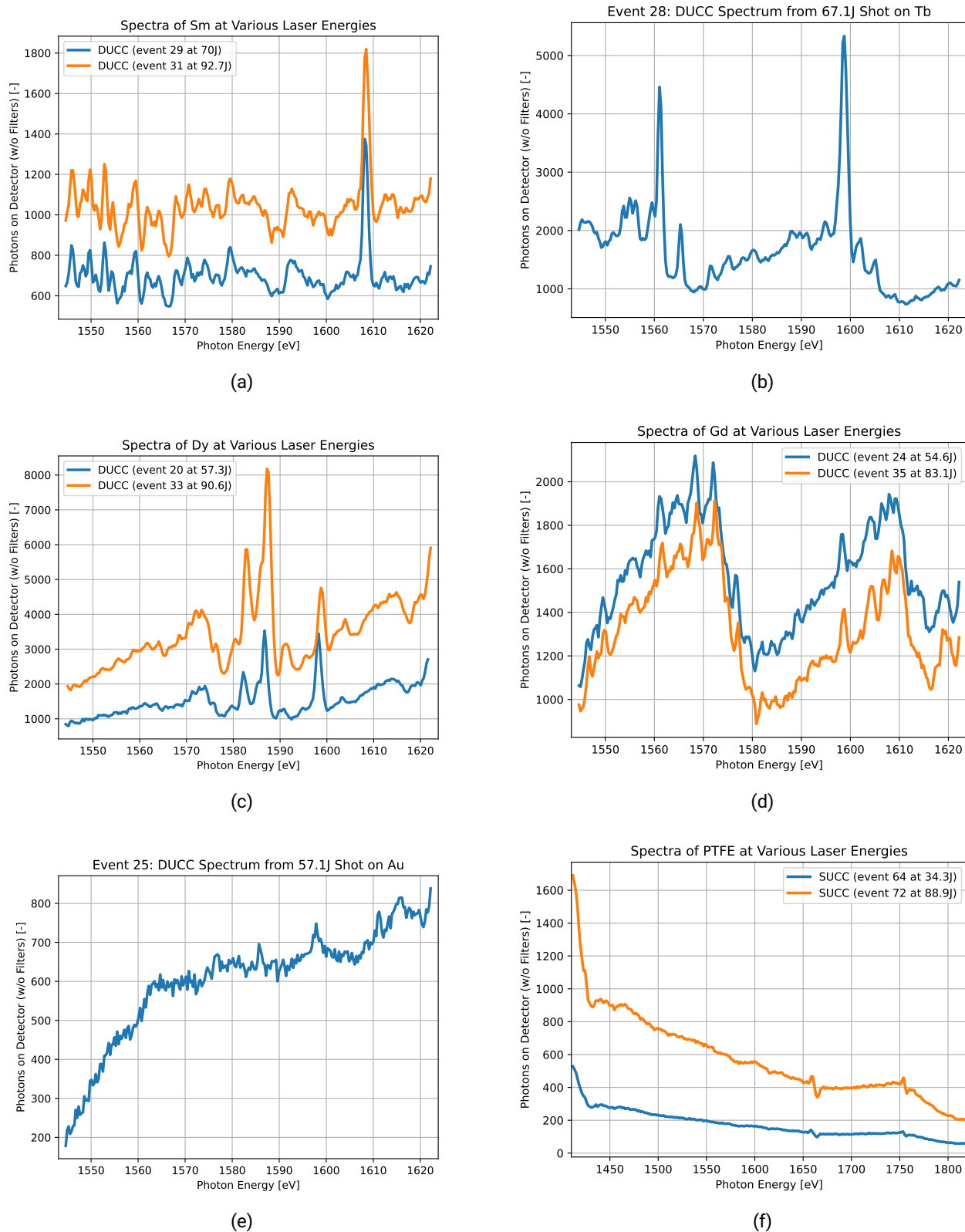
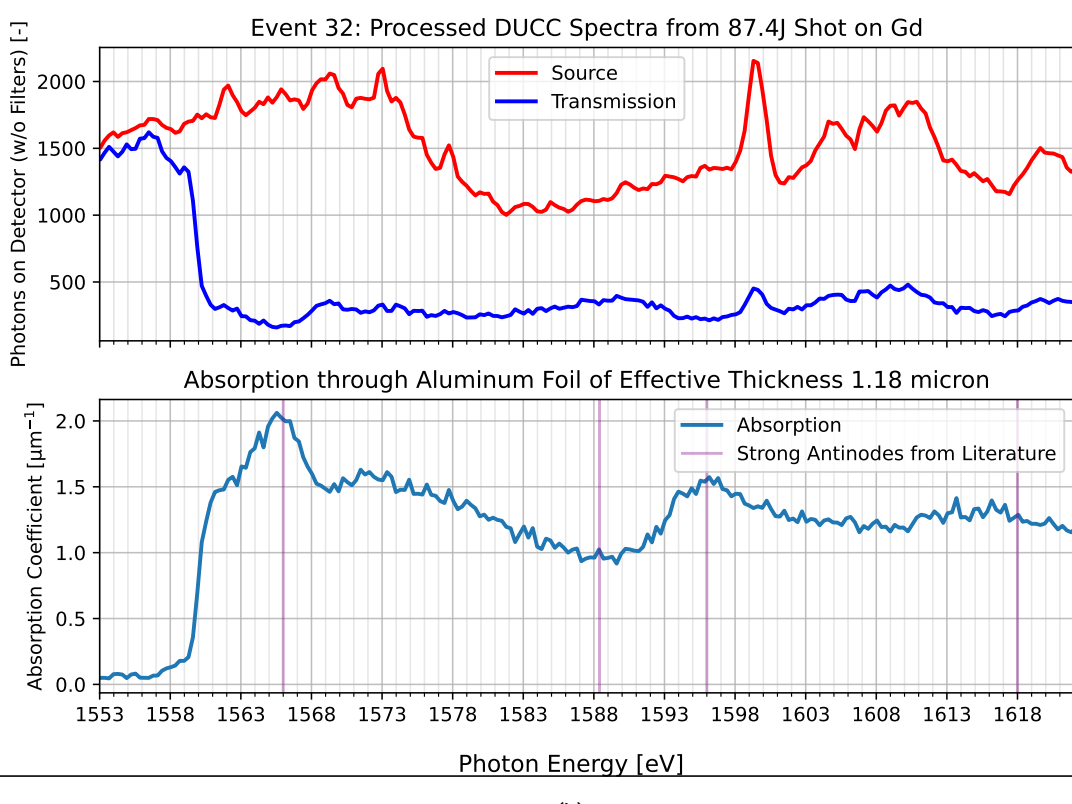
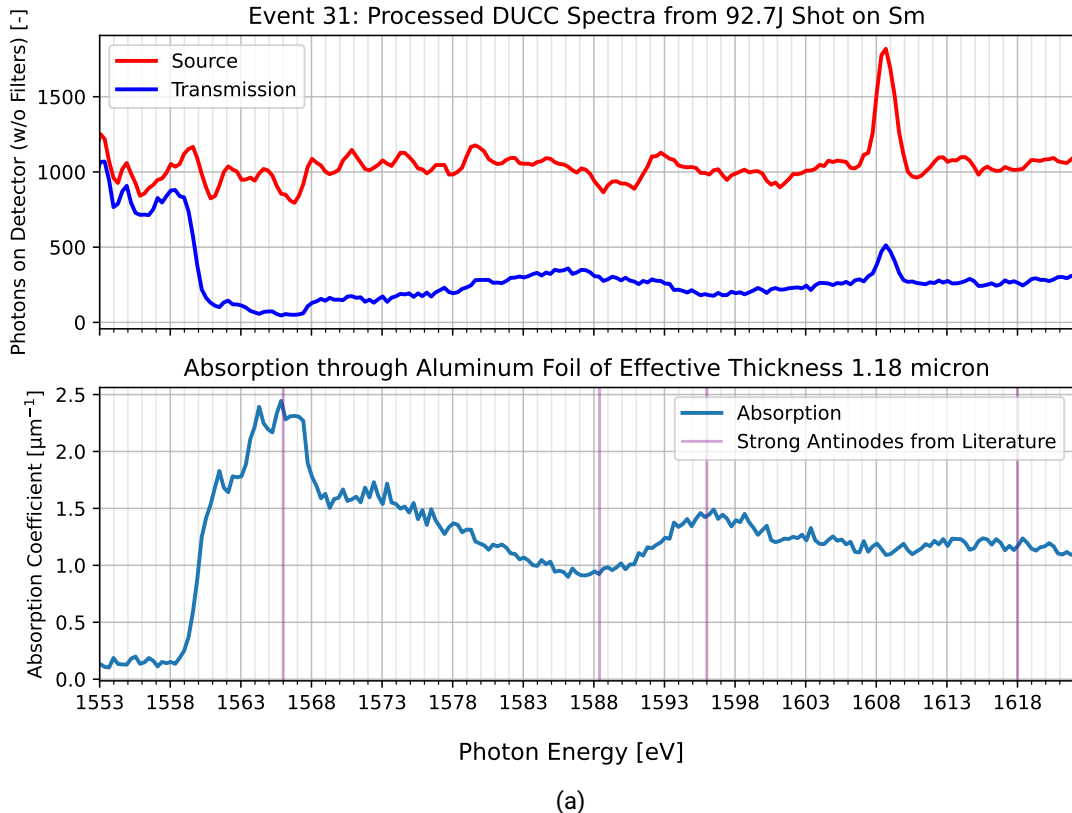
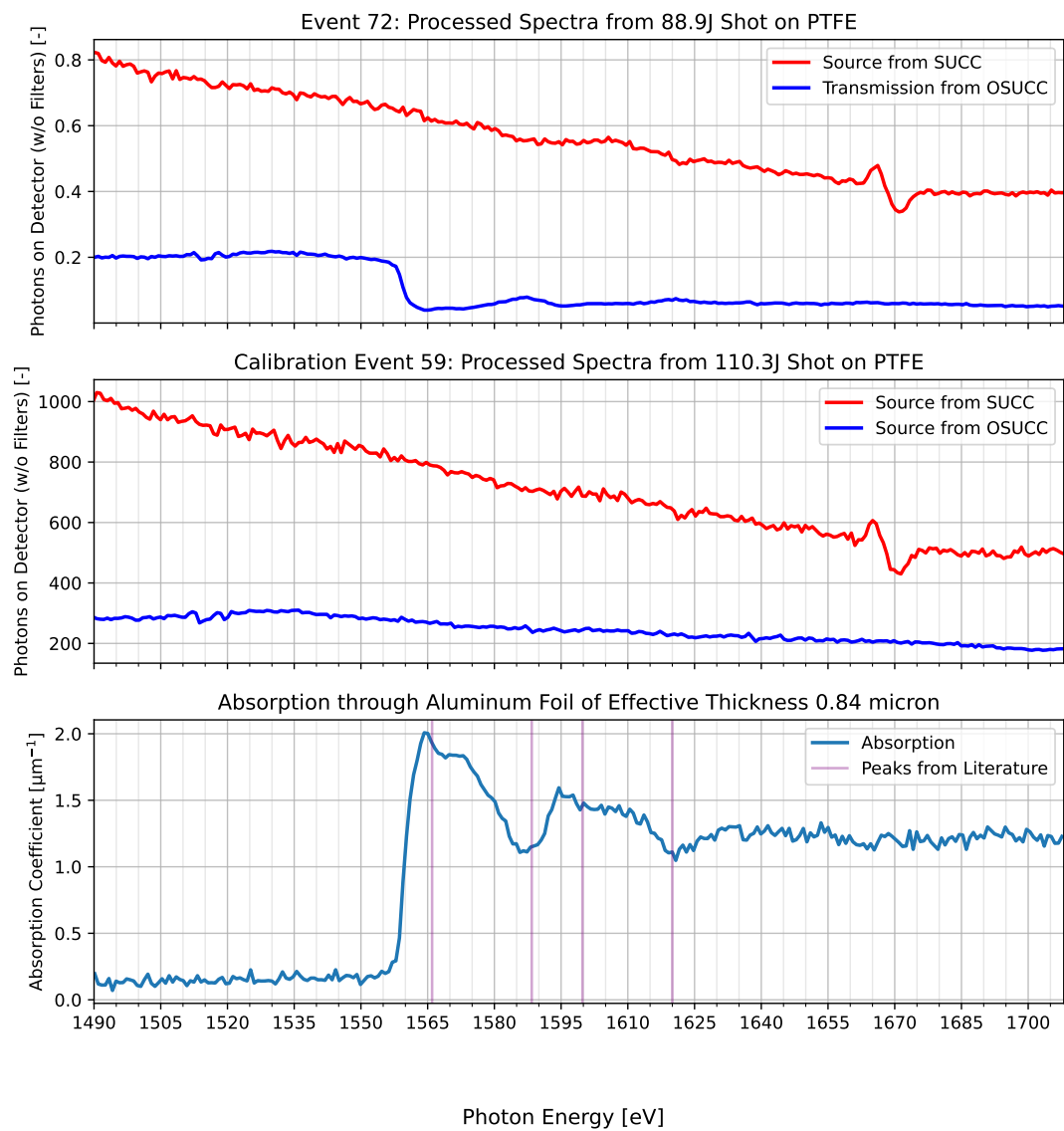


Figure 6.3.



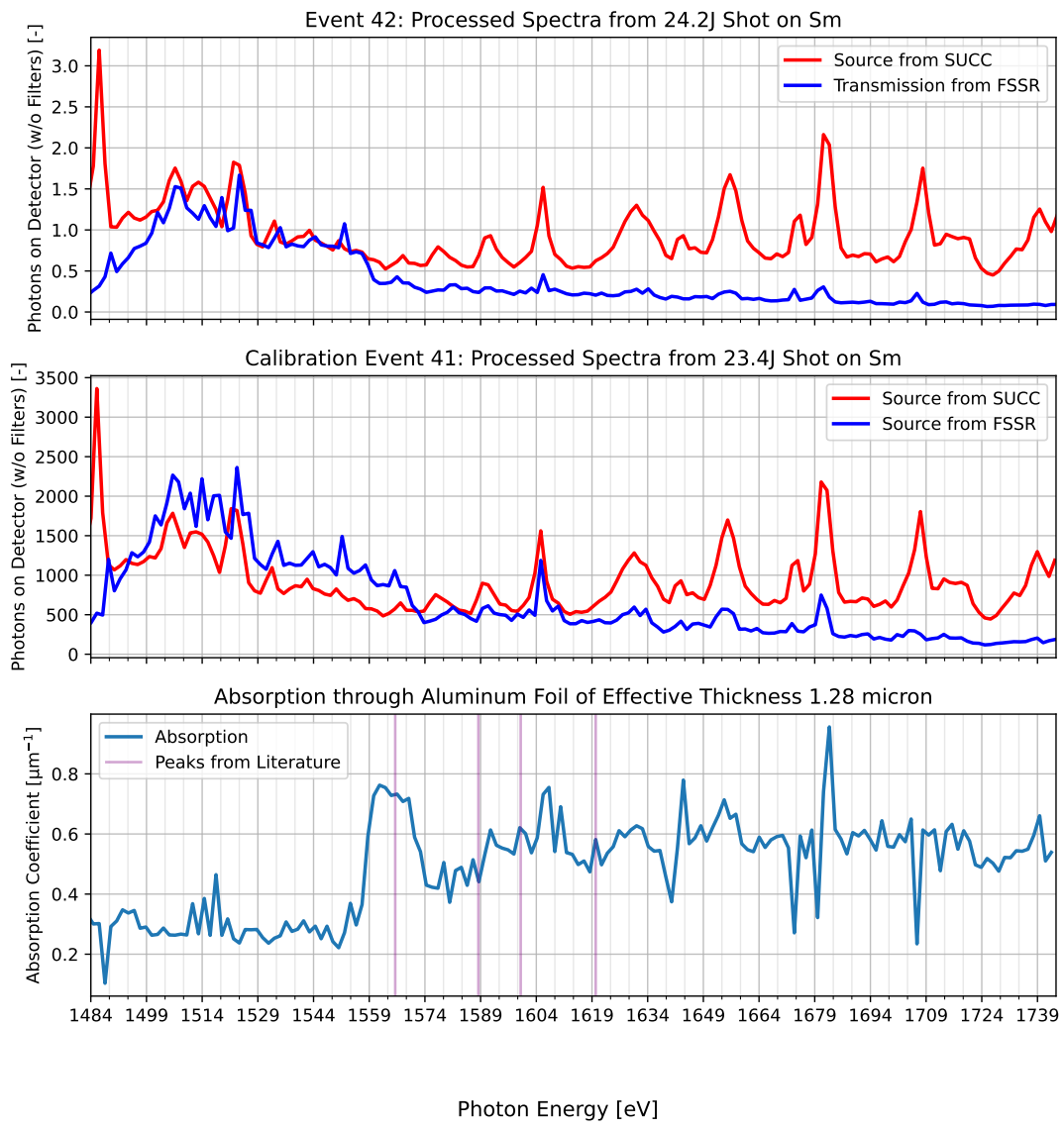
6.1.2. Absorption Spectra





Photon Energy [eV]

Figure 6.5.



Photon Energy [eV]

Figure 6.6.

6.2. Spectrometer Characterization

6.2.1. Spectral Resolution

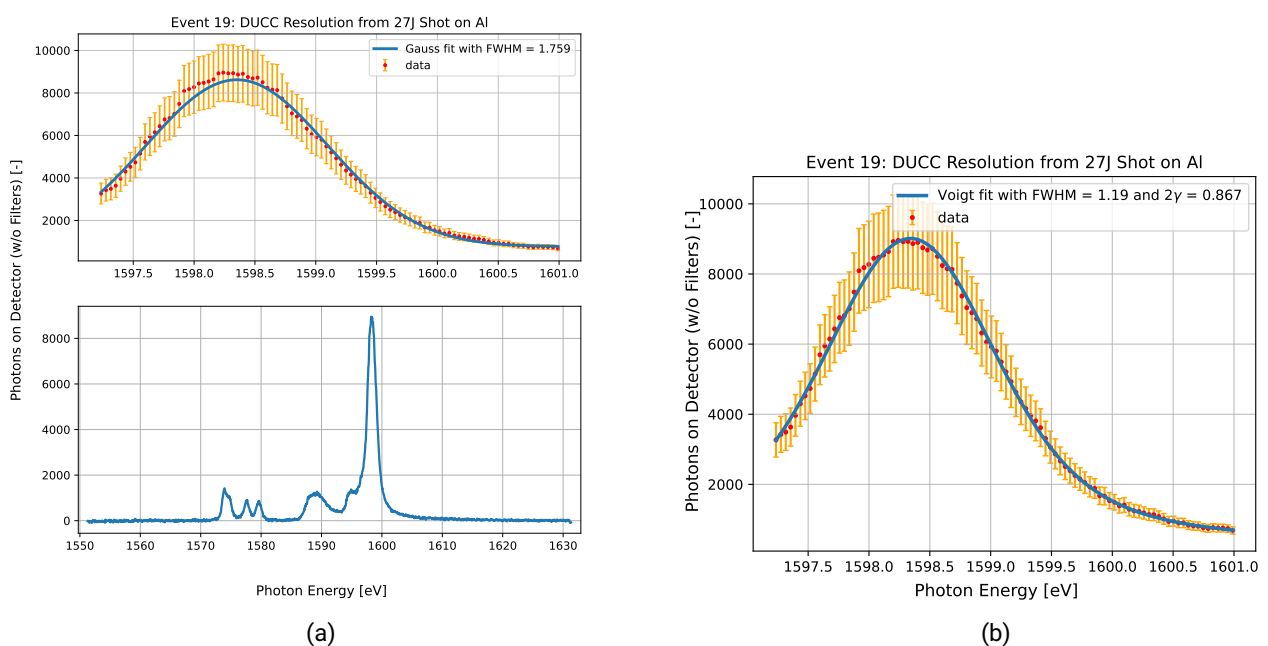


Figure 6.7.

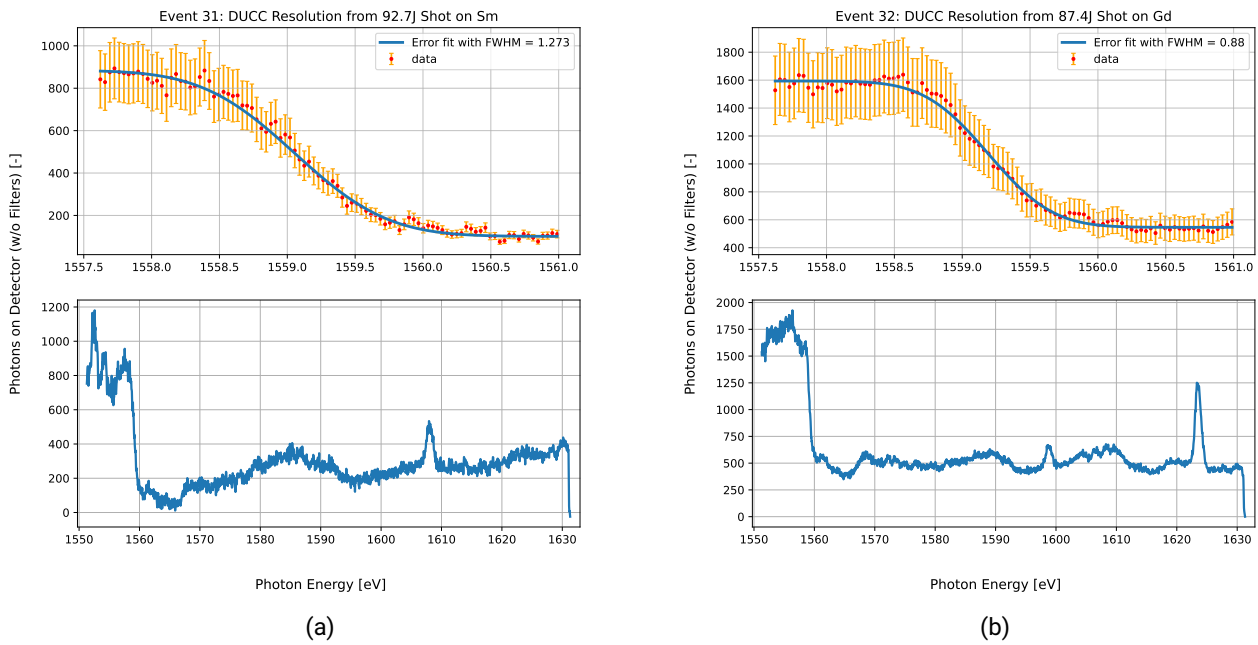


Figure 6.8.

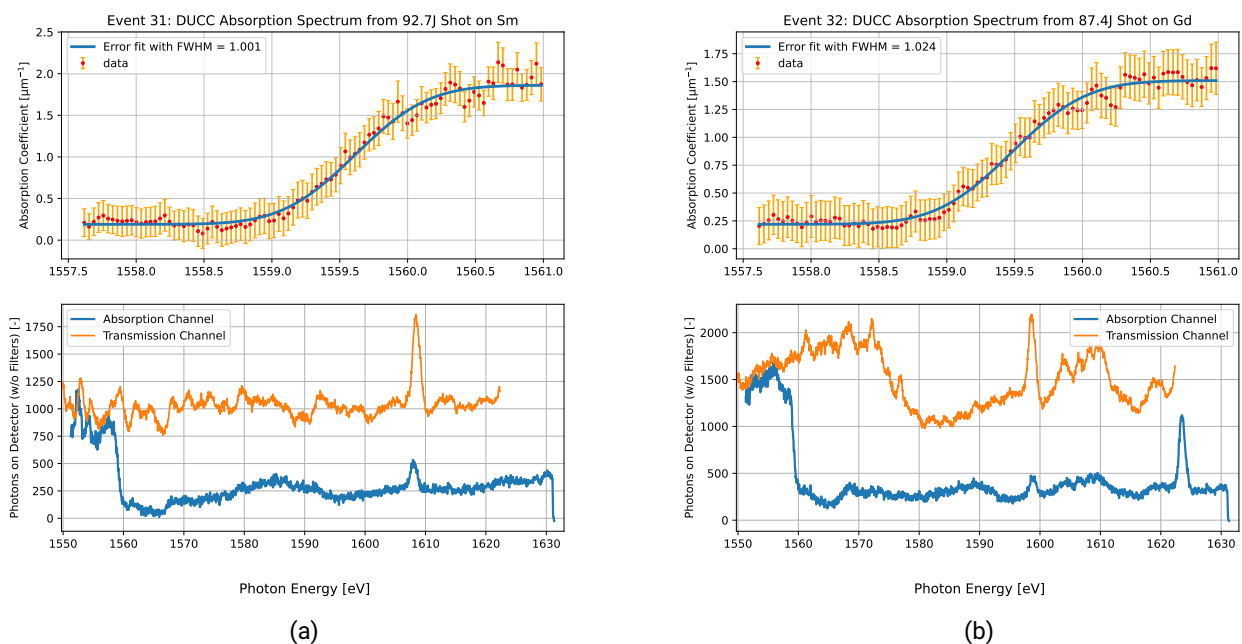
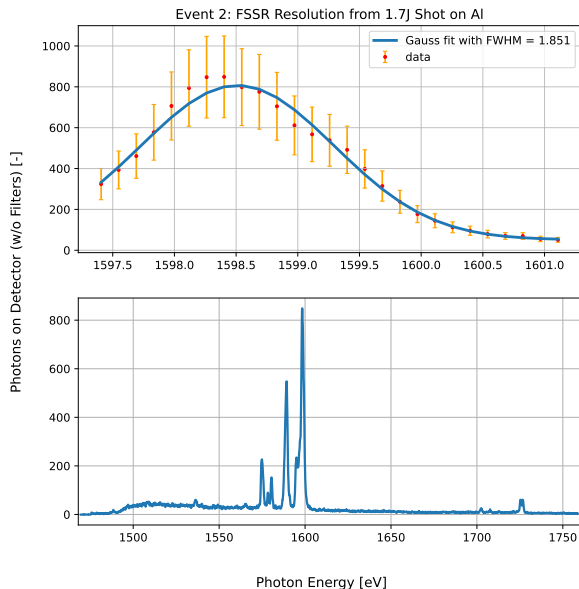
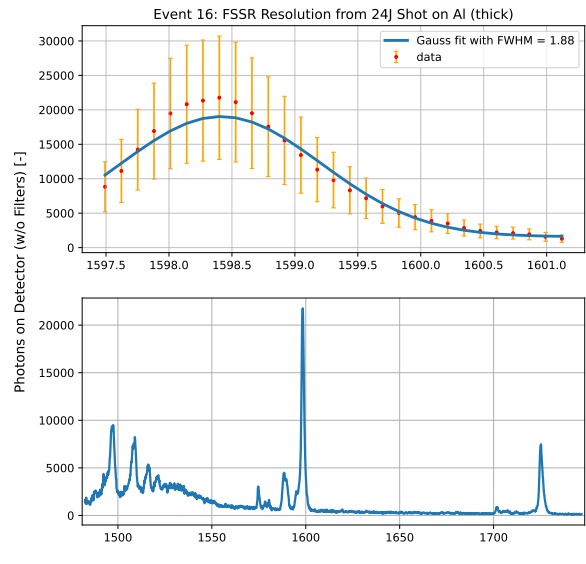


Figure 6.9.

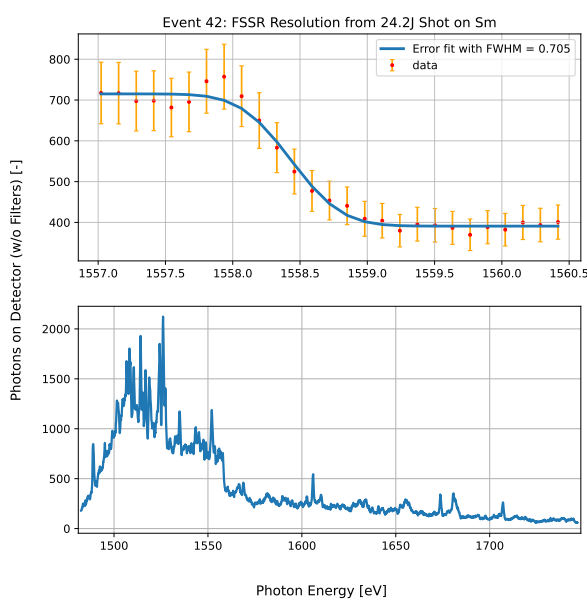


(a)

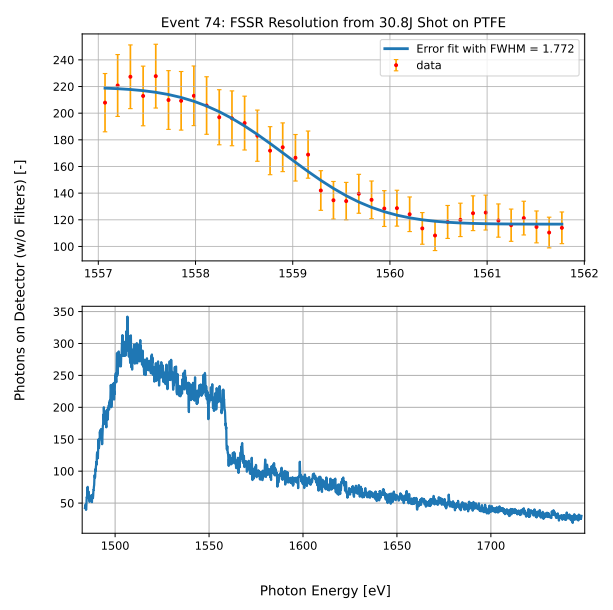


(b)

Figure 6.10.

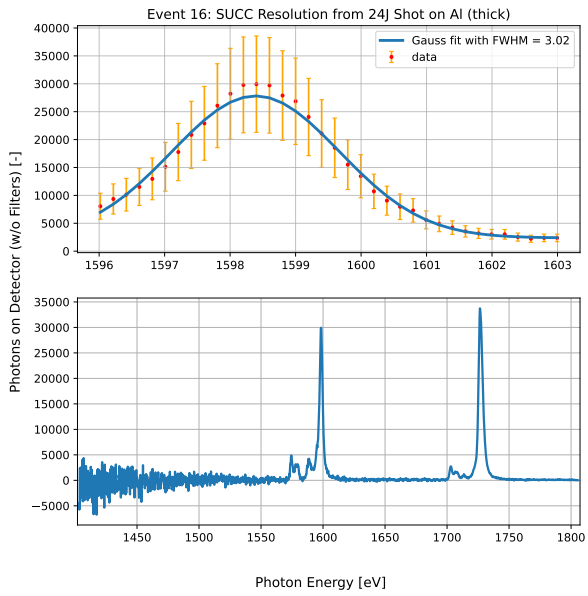


(a)

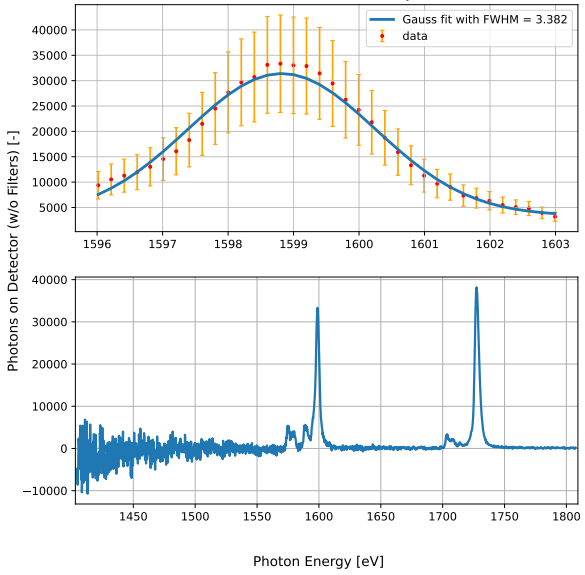


(b)

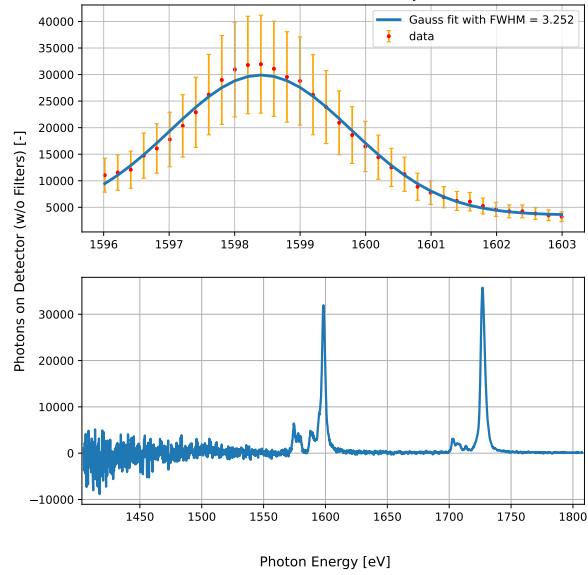
Figure 6.11.



(a)



(b)



(c)

Figure 6.12.

Table 6.1.: Resolution of DUCC. Source size broadening calculated with fitting of knife edge. Types pertain to the kind of feature used to derive the resolution: p is peak (- g is gauss fit, - v is voigt fit), t is transmission, and a is absorption. Doppler broadening is from FLYCHK for $T_e = 1000$ eV and error of it is estimated from comparison to a simulation of $T_e = 500$ eV. I show a result from a voigt fit because it yields a resolution close to the other ones (potential sources of lorentz broadening?). Spec resolution is the final resolution resulting from the Entfaltung.

Event	Type	Gauss FWHM	Source Broadening	Doppler	Spec Resolution
19	p-g	1.7585 ± 0.0007	0.454 ± 0.0339	0.474 ± 0.1	1.6315 ± 0.0306
19	p-v	1.1897 ± 0.0179	0.454 ± 0.0339	0.474 ± 0.1	0.9922 ± 0.0546
31	t	1.2725 ± 0.0038	0.6362 ± 0.0046	-	1.1021 ± 0.0051
31	a	1.0009 ± 0.0062	0.5694 ± 0.0087	-	0.823 ± 0.0096
32	t	0.8795 ± 0.0073	0.5216 ± 0.0053	-	0.7082 ± 0.0099
32	a	1.0244 ± 0.0085	0.5125 ± 0.0034	-	0.887 ± 0.01

Table 6.2.: Resolution of FSSR. Same as DUCC for the most part, except that source broadening is negligible.

Event	Type	Gauss FWHM	Source Broadening	Doppler	Spec Resolution
2	p-g	1.8511 ± 0.0057	-	0.474 ± 0.1	1.7894 ± 0.0271
16	p-g	1.8804 ± 0.0255	-	0.474 ± 0.1	1.8197 ± 0.0371
74	t	1.7719 ± 0.1053	-	-	1.7719 ± 0.1053
42	t	0.7046 ± 0.0268	-	-	0.7046 ± 0.0268

Table 6.3.: Resolution of SUCC. Only Gauss peak fits as no transmission shots. Tried estimating a higher doppler broadening error as some values I calculated/found are very different.

Event	Type	Gauss FWHM	Source Broadening	Doppler	Spec Resolution
16	p-g	3.0196 ± 0.0161	1.3582 ± 0.0990	0.474 ± 0.2	2.6549 ± 0.0646
18	p-g	3.3821 ± 0.0326	1.2174 ± 0.1609	0.474 ± 0.2	3.1196 ± 0.0782
19	p-g	3.2522 ± 0.0275	1.7913 ± 0.2242	0.474 ± 0.2	2.6727 ± 0.1580

6.2.2. Integrated Reflectivity Ratio

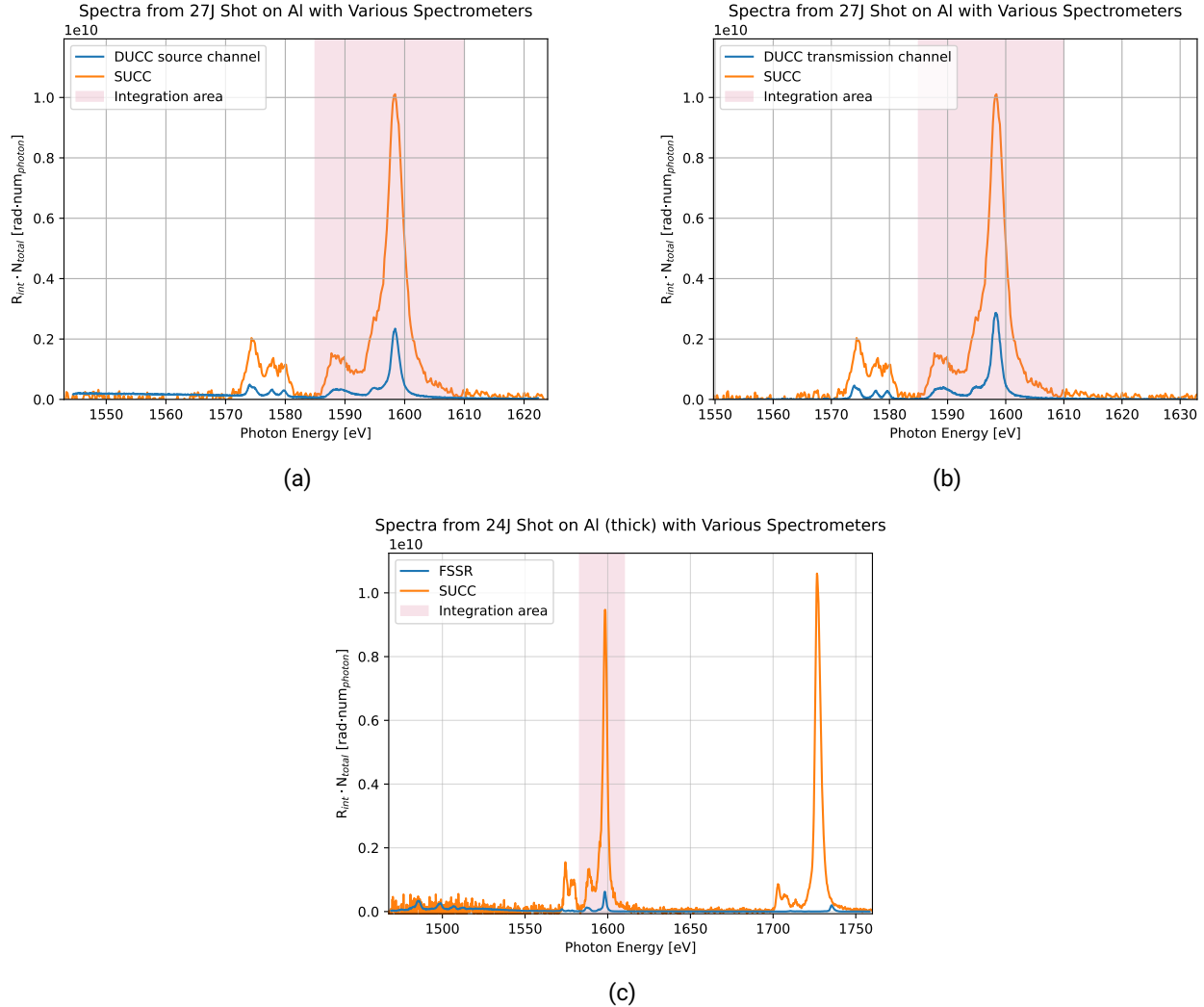


Figure 6.13.

Table 6.4.: Ratio of R_{int} . DUCC_t means transmission channel of DUCC, DUCC_s is the source channel.

Event	Spectrometer	Literature Value	Experimental Ratio
19	DUCC _t /SUCC	0.5	0.884 ± 0.044
19	DUCC _s /SUCC	0.5	0.773 ± 0.038
16	FSSR/SUCC	0.67	0.068 ± 0.016



6.3. Setup Validation

6.3.1. Conversion Efficiency of He- α Line of Aluminum

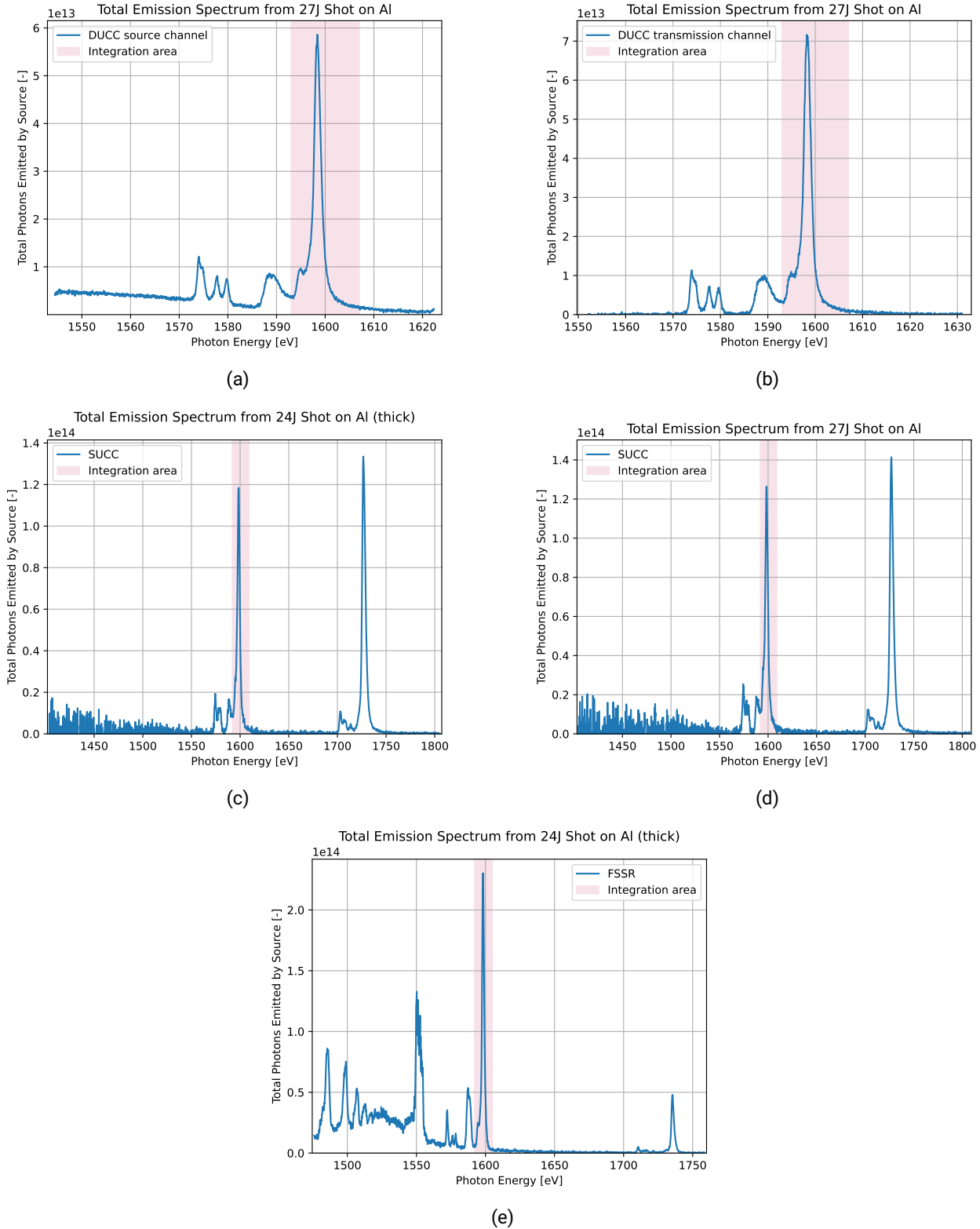


Table 6.5.: CE of Al He- α line. DUCC_{*t*} means transmission channel of DUCC, DUCC_{*s*} is the source channel. FSSR_{*artem*} is calculated by getting the total emitted photons by using a reflectivity curve simulated by Artem.

Event	Spectrometer	CE
19	DUCC _{<i>t</i>}	0.044719±0.022377
19	DUCC _{<i>s</i>}	0.037482±0.018754
16	FSSR	0.00222±0.001122
16	FSSR _{<i>artem</i>}	0.04346±0.00319
16	SUCC	0.025576±0.012854
19	SUCC	0.027375±0.01375

6.3.2. He- α and Ly- α Line Ratio of Aluminum

7. Results and Discussion

8. Outlook

THIS CHAPTER IS THE SAME AS IN THE PROPOSAL AND WILL BE COMPLETELY REWRITTEN.

To close this work, I will summarize the results and most important features of the spectrometer designs, as well as elaborate on the preparatory experiment to be conducted in the summer of 2023 at HHT.

Two spectrometers were designed and built in the course of this work, namely the Dual Unbent Crystal Spectrometer (DUCC) and the Focusing Spectrograph with Spatial Resolution in 1 Dimension (FSSR-1D). The DUCC aims to resolve XANES around the Al K-edge and leverages a dual crystal design to simultaneously capture a transmission and backlighter spectrum on one detector. The FSSR-1D is designed to measure EXAFS and sports a spherically bent crystal, which enables spectral focusing and 1D spatial imaging onto the detector, significantly reducing background and increasing signal strength. The designs were informed by the considerations outlined in chapter 4.1, which included: covering the energy ranges relevant to XANES and EXAFS respectively, limitations imposed by the WDM sample size due to the uniformity requirements of the heavy-ion heating, goals for the spectral resolution for observing XANES and EXAFS, requiring sufficient intensity on the detector, and keeping the physical size low enough to fit in the setup. Both spectrometers fulfilled all the considerations, with the DUCC covering an energy range of 1541 eV - 1618 eV and leading to a sample size of 0.51 mm, a central Bragg angle of 47.58°, and a spectrometer length of 235.17 mm. The FSSR-1D records in an energy range of 1465 eV - 1755 eV and gives a sample size of 0.76 mm, a central Bragg angle of 51.36°, and a spectrometer length of 404.30 mm. Using mmpxrt simulations, the energy resolutions were determined, which included an estimation of the crystal properties' contribution to the DUCC resolution, resulting in $\Delta E_{total} = 0.703$ eV for the DUCC and $\Delta E_{total} = 3.097$ eV for the FSSR-1D. The largest contribution to ΔE_{total} originated from the source broadening for the DUCC and the crystal properties for the FSSR-1D. In both cases, the detector's influence on the resolution was negligible. Finally, the spectrometers' mechanical design was developed in *Autodesk Inventor 2020*. Each spectrometer took into account experimental conditions by shielding the sensitive crystals and camera chips, where the chips are further insulated from visible light. The design includes necessary parts to fully align the spectrometers in the experimental setup, which must be especially exacting for the FSSR-1D.

In the coming experiment with the PHELIX laser-only setup, the spectrometers will be utilized to observe X-ray Absorption Fine-Structure (XAFS) at and around the aluminum K-edge. The Al samples will be backlit by x-ray emission from laser-driven plasmas, which will be generated by irradiating backlighters of various materials with ns-pulses from the PHELIX laser. The experiment has three main goals: 1) Test the experimental setup as a whole, 2) Investigate various backlighter targets for use in absorption spectroscopy, 3) Assess the spectrometers. Considering the second goal, it has to be taken into account that the backlighter characteristics, such as brightness and spectral shape, directly influence the requirements for the spectrometers. Therefore, the question of the best backlighter and spectrometer cannot be answered independently. The experiment will consequently be focused on gathering data for different backlighter-spectrometer combinations, from which a joint assessment can be made. As for the third goal, the spectrometer performance in itself will be investigated by using line emission from Al targets for spectral

calibration as well as determining the energy resolution. Additionally, the relative reflectivity of the crystals, necessary for absorption spectrum processing, will be assessed by using two spectrometers per shot.

In conclusion, the careful design and detailed analysis of the spectrometer performance, independent of and in relation to the backlighters, will be an important contribution to the optimization of XAFS of heavy-ion heated aluminum using laser-driven plasmas as x-ray sources.

Bibliography

- [1] D. Riley, Warm Dense Matter: Laboratory Generation and Diagnosis, IOP Publishing (2021), doi: 10.1088/978-0-7503-2348-2.
- [2] K. Falk, Experimental methods for warm dense matter research, High Power Laser Science and Engineering, **6**:e59 (2018), doi:10.1017/hpl.2018.53.
- [3] F. Graziani *et al.*, Frontiers and challenges in warm dense matter, volume 96, Springer Science & Business (2014).
- [4] M. Koenig *et al.*, Progress in the study of warm dense matter, Plasma Physics and Controlled Fusion, **47**(12B):B441 (2005), doi:10.1088/0741-3335/47/12B/S31.
- [5] G. Collins *et al.*, Measurements of the equation of state of deuterium at the fluid insulator-metal transition, Science, **281**(5380):1178–1181 (1998), doi:10.1126/science.281.5380.1178.
- [6] N. Tahir *et al.*, Planetary physics research at the Facility for Antiprotons and Ion Research using intense ion beams, The European Physical Journal Plus, **137**(2):273 (2022), doi:10.1140/epjp/s13360-022-02476-2.
- [7] V. Bagnoud *et al.*, Commissioning and early experiments of the PHELIX facility, Applied Physics B, **100**:137–150 (2010), doi:10.1007/s00340-009-3855-7.
- [8] M. Millot *et al.*, Nanosecond X-ray diffraction of shock-compressed superionic water ice, Nature, **569**(7755):251–255 (2019), doi:10.1038/s41586-019-1114-6.
- [9] M. Altarelli, The European X-ray free-electron laser facility in Hamburg, Nuclear Instruments and Methods in Physics Research Section B: Beam Interactions with Materials and Atoms, **269**(24):2845–2849 (2011), doi:10.1016/j.nimb.2011.04.034.
- [10] K. Schoenberg *et al.*, High-energy-density-science capabilities at the Facility for Antiproton and Ion Research, Physics of plasmas, **27**(4):043103 (2020), doi:10.1063/1.5134846.
- [11] R. Torchio *et al.*, Probing local and electronic structure in Warm Dense Matter: single pulse synchrotron x-ray absorption spectroscopy on shocked Fe, Scientific reports, **6**(1):1–8 (2016), doi: 10.1038/srep26402.
- [12] R. W. Lee *et al.*, Finite temperature dense matter studies on next-generation light sources, JOSA B, **20**(4):770–778 (2003), doi:10.1364/JOSAB.20.000770.
- [13] M. Newville, Fundamentals of XAFS, Reviews in Mineralogy and Geochemistry, **78**(1):33–74 (2014), doi:10.2138/rmg.2014.78.2.
- [14] T. Hall *et al.*, Experimental observation of ion correlation in a dense laser-produced plasma, Physical review letters, **60**(20):2034 (1988), doi:10.1103/PhysRevLett.60.2034.

- [15] A. Levy *et al.*, Double conical crystal x-ray spectrometer for high resolution ultrafast x-ray absorption near-edge spectroscopy of Al K edge, *Review of Scientific Instruments*, **81**(6):063107 (2010), doi:10.1063/1.3441983.
- [16] O. Peyrusse *et al.*, K-edge Absorption spectra in Warm Dense Matter, in *AIP Conference Proceedings*, volume 1161, 200–206, American Institute of Physics (2009), doi:10.1063/1.3241191.
- [17] A. Fontaine *et al.*, Soft X-ray absorption and EXAFS on the K edge of aluminium, *Journal of Physics F: Metal Physics*, **9**(10):2143 (1979), doi:10.1088/0305-4608/9/10/023.
- [18] A. Lévy *et al.*, X-ray absorption for the study of warm dense matter, *Plasma Physics and Controlled Fusion*, **51**(12):124021 (2009), doi:10.1088/0741-3335/51/12/124021.
- [19] L. Dubrovinsky *et al.*, In situ X-ray study of thermal expansion and phase transition of iron at multimegarbar pressure, *Physical Review Letters*, **84**(8):1720 (2000), doi:10.1103/PhysRevLett.84.1720.
- [20] N. Tahir *et al.*, Studies of high-energy density states using isochoric heating of matter by intense heavy ion beams: the HEDgeHOB Collaboration, *Physica Scripta*, **2008**(T132):014023 (2008), doi:10.1088/0031-8949/2008/T132/014023.
- [21] Ringbeschleuniger SIS18 – der Rekordhalter, URL <https://www.gsi.de/forschungbeschleuniger/beschleunigeranlage/ringbeschleuniger>.
- [22] D. Varentsov, HHT Experimental Area, URL https://www.gsi.de/work/forschung/appamml/plasmaphysikphelix/anlagen_bei_sis18_hht.
- [23] D. Hoffmann *et al.*, Frontiers of dense plasma physics with intense ion and laser beams and accelerator technology, *Physica Scripta*, **2006**(T123):1 (2006), doi:10.1088/0031-8949/2006/t123/001.
- [24] O. Renner and F. Rosmej, Challenges of x-ray spectroscopy in investigations of matter under extreme conditions, *Matter and Radiation at Extremes*, **4**(2):024201 (2019), doi:10.1063/1.5086344.
- [25] A. Mottana and A. Marcelli, The historical development of X-ray Absorption Fine Spectroscopy and of its applications to Materials Science, *A Bridge between Conceptual Frameworks: Sciences, Society and Technology Studies*, 275–301 (2015), doi:10.48550/arXiv.1312.5295.
- [26] R. Eason *et al.*, Improved laser-EXAFS studies of aluminium foil, *Journal of Physics C: Solid State Physics*, **17**(28):5067 (1984), doi:10.1088/0022-3719/17/28/022.
- [27] W. Bragg and W. Bragg, The X-ray spectrometer, *Nature*, **94**(2347):199–200 (1914).
- [28] H.-J. Kunze, *Introduction to plasma spectroscopy*, volume 56, Springer Science & Business Media (2009), doi:<https://doi.org/10.1007/978-3-642-02233-3>.
- [29] Q. Yang *et al.*, Focusing X-ray spectrograph with spatial resolution and uniform dispersion, *Nuclear Instruments and Methods in Physics Research Section A: Accelerators, Spectrometers, Detectors and Associated Equipment*, **634**(1):52–58 (2011), doi:10.1016/j.nima.2011.01.032.
- [30] O. Renner *et al.*, Vertical variant of a double channel-cut crystal spectrometer for investigation of laser-generated plasmas, *Review of scientific instruments*, **70**(7):3025–3031 (1999), doi:10.1063/1.1149863.
- [31] G. Hölzer *et al.*, Flat and spherically bent muscovite (mica) crystals for X-ray spectroscopy, *Physica Scripta*, **57**(2):301 (1998), doi:10.1088/0031-8949/57/2/029.

- [32] F. Blasco *et al.*, Portable, tunable, high-luminosity spherical crystal spectrometer with an x-ray charge coupled device, for high-resolution x-ray spectromicroscopy of clusters heated by femtosecond laser pulses, *Review of scientific instruments*, **72**(4):1956–1962 (2001), doi:10.1063/1.1355273.
- [33] H. H. Johann, Die erzeugung lichtstarker röntgenspektren mit hilfe von konkavkristallen, *Zeitschrift für Physik*, **69**:185–206 (1931), doi:10.1007/BF01798121.
- [34] P. Monot *et al.*, High-sensitivity, portable, tunable imaging X-ray spectrometer based on a spherical crystal and MCP, *Nuclear Instruments and Methods in Physics Research Section A: Accelerators, Spectrometers, Detectors and Associated Equipment*, **484**(1-3):299–311 (2002), doi:10.1016/S0168-9002(01)01991-X.
- [35] A. Y. Faenov *et al.*, High-performance x-ray spectroscopic devices for plasma microsources investigations, *Physica Scripta*, **50**(4):333 (1994), doi:10.1088/0031-8949/50/4/003.
- [36] T. Pikuz *et al.*, Bragg X-ray optics for imaging spectroscopy of plasma microsources, *Journal of X-ray Science and Technology*, **5**(3):323–340 (1995), doi:10.1006/jxra.1995.0009.
- [37] T. Döppner *et al.*, High order reflectivity of highly oriented pyrolytic graphite crystals for x-ray energies up to 22 keV, *Review of Scientific Instruments*, **79**(10):10E311 (2008), doi:10.1063/1.2966378.
- [38] B. Young *et al.*, High-resolution x-ray spectrometer based on spherically bent crystals for investigations of femtosecond laser plasmas, *Review of Scientific Instruments*, **69**(12):4049–4053 (1998), doi:10.1063/1.1149249.
- [39] B. L. Henke, E. M. Gullikson and J. C. Davis, X-ray interactions: photoabsorption, scattering, transmission, and reflection at $E = 50\text{--}30,000 \text{ eV}$, $Z = 1\text{--}92$, *Atomic data and nuclear data tables*, **54**(2):181–342 (1993), doi:10.1006/adnd.1993.1013.
- [40] C. Ferrari *et al.*, Characterization of ammonium dihydrogen phosphate crystals for soft X-ray optics of the Beam Expander Testing X-ray facility (BEaTriX), *Journal of Applied Crystallography*, **52**(3):599–604 (2019), doi:10.1107/S1600576719004631.
- [41] P. Rajesh and P. Ramasamy, Growth and characterization of large size ADP single crystals and the effect of glycine on their growth and properties, *Optical Materials*, **42**:87–93 (2015), doi:10.1016/j.optmat.2014.12.024.
- [42] M. Alkhimova *et al.*, Determination of spectral reflectivity of spherically bent mica crystals applied for diagnostics of relativistic laser plasmas, in *Journal of Physics: Conference Series*, volume 774, 012115, IOP Publishing (2016), doi:10.1088/1742-6596/774/1/012115.
- [43] G. P. Loisel *et al.*, Measurement and models of bent KAP (001) crystal integrated reflectivity and resolution, *Review of Scientific Instruments*, **87**(11) (2016), doi:10.1063/1.4960149.
- [44] M. Šmíd, X. Pan and K. Falk, X-ray spectrometer simulation code with a detailed support of mosaic crystals, *Computer Physics Communications*, **262**:107811 (2021), doi:10.1016/j.cpc.2020.107811.
- [45] J. Gilfrich, D. Brown and P. Burkhalter, Integral reflection coefficient of X-ray spectrometer crystals, *Applied Spectroscopy*, **29**(4):322–326 (1975), doi:10.1366/00037027577445591.

I. Crystals

The choice of crystal for the spectrometers took several aspects into account:

- **Lattice Spacing:** The lattice spacing must lie in a range that ensures the Bragg condition is fulfilled for reasonable incident angles depending on the spectrometer geometry and the consideration 2 outlined above.
- **Diffraction Order:** Reflection in the first order is preferred, as the lower orders typically display higher reflection efficiency and cover a lower energy range, corresponding to higher intensities from the plasma source compared to intensities at higher energies [24, 34].
- **Bendability:** A bent crystal allows for high intensities on the detector and reduces shot-to-shot fluctuations [15]. It could also potentially offer spatial resolution.
- **Intrinsic Properties:** As discussed in section 2.4, a compromise between a small rocking curve width and sufficiently high integrated reflectivity is required to reach high resolutions while maintaining good luminosity on the detector.
- **Availability:** The crystals themselves must be acquirable.

It is noted that various crystals were considered for each spectrometer, but were gradually eliminated during the initial design development. For example, KAP was considered for the flat crystal geometry, but was rejected since it would lead to a too high spectrometer length. Quartz also came into consideration for the FSSR-1D, but in the end did not allow for a FSSR geometry that fulfilled the experimental requirements.

II. Calculations and Simulations

To investigate the spectrometer properties and validate the design I ran ray tracing simulations, using a self-made simple ray tracing code and the python3 ray tracing code mmpxrt, built by Michal Šmíd at the Helmholtz-Zentrum Dresden-Rossendorf [44]. mmpxrt is specialized for x-ray spectrometers and supports bent crystal geometries.

First, I will discuss the simple ray tracing code and its application in section 4.1. This is followed by the presentation and discussion of the results of the mmpxrt simulations of the DUCC and FSSR spectrometers in sections 4.2 and 4.3 respectively. Finally, I will summarize the results of the simulations and present the expected contributions to the resolution for each spectrometer in section 4.4.

i. Simple Ray Tracing of the Focusing Spectrograph with Spatial Resolution

It should be noted that this code is not, strictly speaking, a full ray tracing program, as the direction and energy of the rays are not randomly chosen. Despite this I will use the term ray tracing in this section for simplicity.

During the design phase of this work, it was unclear how exactly the detector surface should be orientated for the FSSR-1D. In order to directly test this, I made a simple 2D ray tracing code. The calculation of the rays is done by finding the line equation for each ray before and after reflection on the crystal. It then uses the imaging condition in the vertical plane (see eq. 3.2) to find the optimal intersection point with the detector for each photon energy. The ray tracing follows the steps:

1. The initial ray begins at the source, which is assumed to be a point source, and ends at the contact point with the crystal surface. By taking advantage of the known location of the source, set by the geometry of the spectrometer, and the circle equation of the crystal curvature, the contact point can be calculated for a given Bragg angle, and therefore energy.
2. Using the calculated contact point and the fact that the ray is reflected on the crystal, the line equation of the reflected ray is determined.
3. The reflected ray is propagated until it reaches the distance b given by the imaging condition in the vertical plane. a is calculated by the length of the initial ray. This final point is denoted as the imaging point of the ray.
4. Finally, the detector line is drawn out along the line of best fit of the set of imaging points for a range of energies, where all rays that do not land on the crystal are filtered out.

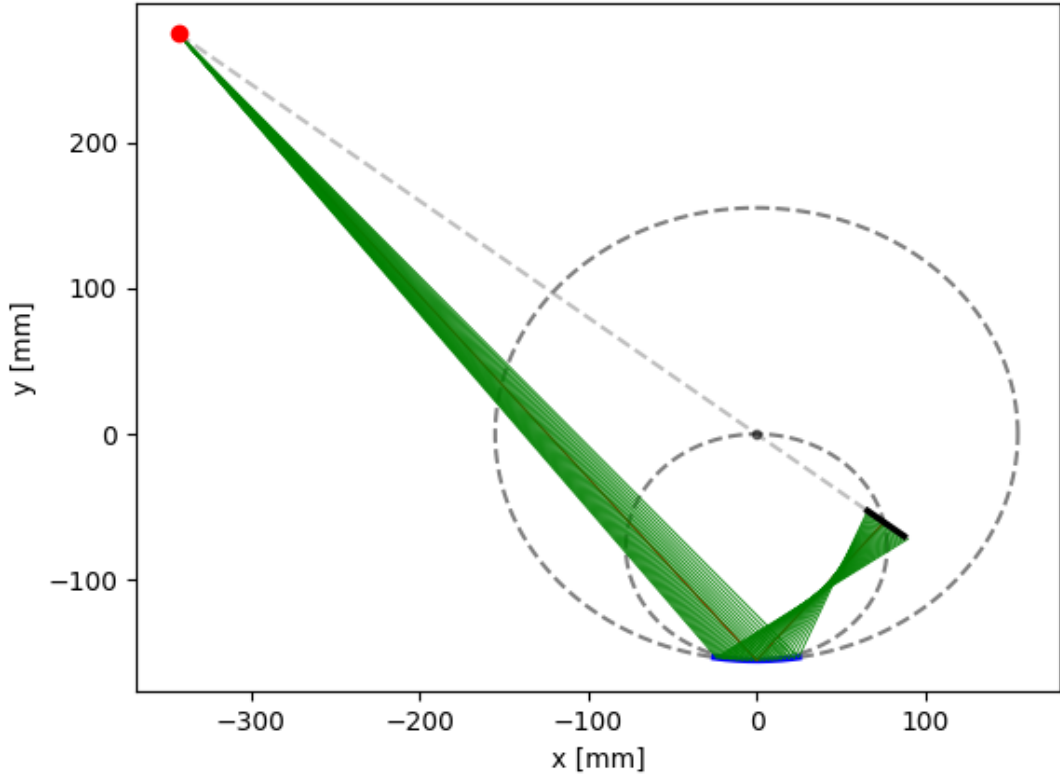


Figure II.1.: Simple ray tracing of the FSSR-1D with a mica crystal with second order diffraction, where $R = 155$ mm, $E_0 = 1600$ eV and $a_0 = 549.7$ mm. The detector length in dispersive direction is 27.6 mm and the crystal length is 50 mm. The red dot represents the source and the red ray is the central ray. The remaining rays are shown in green. The crystal is in blue and the detector in black. The dotted circles depict the crystal curvature and the RC respectively. Finally, the black dot shows the center of the crystal curvature circle.

The code delivers the diagram seen in fig. II.1, where the parameters of the final FSSR-1D are used. Notably, the detector line lies exactly on a symmetry axis of the circle drawn out from the crystal curvature, even though no explicit symmetry relations were used in the calculations. This supports the optimal orientation outlined in section 3.3. In addition, the angle of the central ray to the detector line is 90° , as expected for the FSSR-1D geometry.

To note is that this geometry has many degrees of freedom when fine tuning the spectrometer. As such, it's simpler to set a parameter first, then adjust the others accordingly. In this work, I set the central ray to be incident on the center of the crystal, meaning the central energy E_0 corresponding to this ray doesn't lie in the center of the energy range due to the off-axis source location (relative to the spherical crystal optical axis). Therefore, the easiest way to fine tune the energy range, limited by detector position and size as well as crystal position and size, is to slightly shift the detector location along the symmetry axis mentioned above. In this case, I chose the top end of the detector (positive y direction) to correspond with the topmost ray (lowest energy ray) reflected from the crystal, as seen in fig. II.1. This choice covered the largest possible energy range with this setup. With the offset and orientation set, the placement of the detector is determined.

This code is applicable for all FSSR geometries and can be used to quickly determine the optimal detector placement for any FSSR.

ii. Simulation of the Focusing Spectrograph with Spatial Resolution

I simulated the FSSR-1D with the same parameters as in the final design (see table 4.1) using mmpxrt. In this section I will discuss the quantities relevant to the validation of the final design. For more details about each graph and result of the simulation, refer to [44].

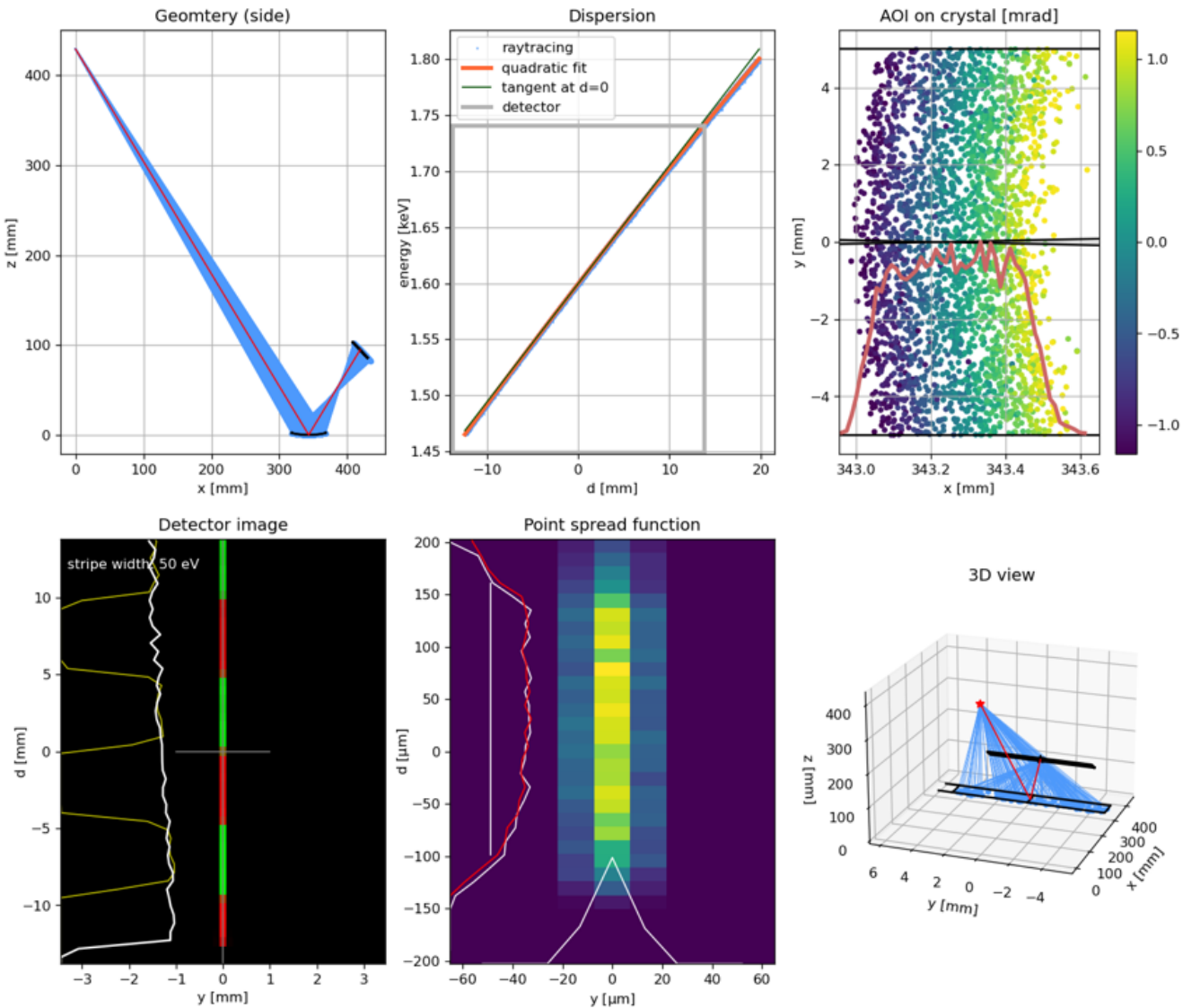


Figure II.2.: Graphical results of mmpxrt simulation of the FSSR-1D, wherein the point spread function used to find the energy resolution is in the bottom middle.

Mmpxrt v. 1.13

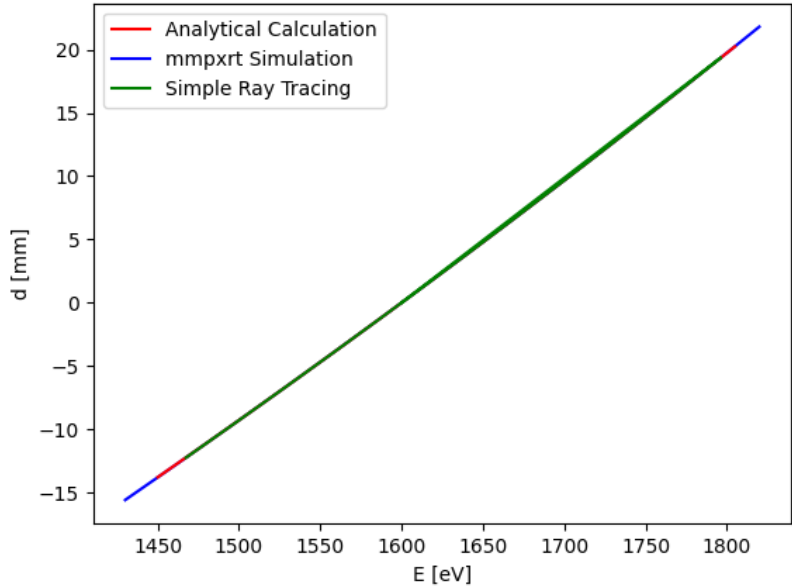
FSSR-1D

Energy range
 central E: 1600 eV
 E range max.: 336 eV
 i.e. reflecting rays in range: 1465 - 1800 eV
 E range fwhm: 330 eV
 E range on detector: 292 eV

$$\text{dispersion: } E[\text{eV}] = -0.02193d^2 + 10.57d + 1600$$

Energy resolution
 vertical spread from rms: 0.214 mm
 - energy resolution: 2.264 eV
 vertical spread from fwhm: 0.279 mm
 - energy resolution: 2.954 eV
 vert. spr. narrow (fwhm): 0.260 mm
 - energy resolution: 2.748 eV
 dispersion per px: 0.1 eV/px

Source size broadening
 magnification in spectral direction: 0.01
 source size broadening: 0.09 eV/mm



(a) Numerical results of mmpxrt simulation of FSSR-1D with some quantities removed for clarity.

(b) Dispersion of the FSSR-1D calculated with three different methods.

Figure II.3.: (a): Results of simulation of the FSSR-1D with the parameters as in fig. II.1. Simulated using mmpxrt [44]. (b): Comparison of dispersion. Energy range was extended for the simple ray tracing and analytical results to render them visible on the graph.

To run the ray tracing simulation, a number of parameters needed to be input. These include the geometry dependent parameters like radius of crystal curvature and source-crystal distance, among others, along with settings pertaining to the simulation and source/crystal properties. I set the simulation settings according to limitations of the computer and code, where the most important is the parameter `p['simulation']['numerical_intersect_halving']=1`, which increases the runtime but is necessary for simulating curved crystals. As for the source and crystal properties, I set the source to be a cube with length of 0.1 mm and the crystal as a monocrystal with a rocking curve width of 2322 μrad and an integrated reflectivity of 28.9 μrad , as typical values for mica [31].

To assess the accuracy of the simulation, I will first look at the dispersion. I determined the dispersion using three different techniques and graphed them together in fig. II.3b. The simple ray tracing calculation was done by finding d through the absolute distance between the imaging points of a given ray and the central ray. This is an excellent approximation, as the detector line follows the line of imaging points almost exactly, with negligibly small deviations on the order of 10^{-13} mm. For the analytical calculation I used the relation in eq. 3.16. The simulation dispersion is found in fig. II.3a, where one need only take the inverse. It's immediately clear that the results show extremely good agreement. In fact, the lines overlap almost perfectly. This speaks for the validity of all three methods. Furthermore, the dispersion is, as desired, approximately linear over the energy range covered by the detector, as apparent in the fit of the analytical formula

$$d(E) = 1.932 \cdot 10^{-5} \text{ mm/eV}^2 \cdot E^2 + 0.03292 \text{ mm/eV} \cdot E - 102.1 \text{ mm} + \mathcal{O}(E^3). \quad (\text{II.1})$$

The simulation recovers an energy range of 1465 - 1757 eV, which is comparable to the range expected from the FSSR-1D design of approximately 1465 - 1755 eV. Additionally, the dispersion per pixel, using a pixel size of 13.5 μm , is reasonable when compared to the estimated value of 0.14 eV/pixel from the analytical formula. The magnification in dispersive direction and source size broadening are also as expected, taking negligibly small values, with the source broadening resulting in $\Delta E = 0.014$ eV, assuming a source size of 150 μm .

Before discussing the energy resolution, an explanation of each type of resolution given in the mmpxrt results is useful (see fig. II.3a). Each of the three resolutions given is derived from the point spread function (PSF) seen in fig. II.2 using different methods. The first value from "vertical spread from rms" is calculated by taking the root-mean-square of the spread of points in the d direction, then multiplying a factor onto it to approximate a gaussian profile. Consequently, this value is not of much immediate use in this work, as it assumes a distribution. The second value from "vertical spread from fwhm" corresponds to the FWHM of the plot of the profile in dispersive (d) direction, integrating over the y direction. As such, this resolution takes into account the full y range shown in the PSF graph. The third value from "vert. spr. narrow (fwhm)" uses the same process as the second value, with the exception of using only the y range shown by two red lines in the PSF graph. In summary, the first value will not be used in this work, while the choice between the second and third value depends on the y range on the detector one wishes to cover. It is important to mention that this energy resolution result takes only the crystal quality into account.

In the case of the FSSR-1D, the most instructive energy resolution is the second one, as the detector is large enough in the vertical direction (6.9 mm) to capture all the rays in the PSF graph. The result $\Delta E = 2.954$ eV is comparable to an estimated value of $\Delta E_{est} = 2.960$ eV, calculated from the rocking curve width $\Delta\theta = 2322 \mu\text{rad}$ with the formula

$$\Delta E_{est} = E(\theta_0) - E(\theta_0 + \Delta\theta), \quad (\text{II.2})$$

where $E(\theta)$ is determined using Bragg's law (see eq. 3.1). The agreement between the estimated and simulated value speaks for the trustworthiness of the result. To note is that this energy resolution depends directly on the crystal quality, and as such can be noticeably different in the experiment.

iii. Simulation of the Dual Unbent Crystal Spectrometer

As with the FSSR-1D, I simulated the DUCC using the parameters as in the design (see section 4.2.1), where only one channel was considered, as the geometry is analogous along both channels.

The source and simulation parameters in mmpxrt were set just as in section ii, with the exception of leaving out the "numerical_intersect_halving" parameter, since the crystal is flat. The geometry parameters were chosen as in the actual design (see table 4.1). The crystal properties were chosen to correspond to a monocrystal with an integrated reflectivity of 2.32 μrad , taken from [40], and rocking curve width of 800 μrad , which was artificially increased from the literature value of 165 μrad [41], since the simulation did not function for too small a $\Delta\theta$, most likely owing to too few reflected rays.

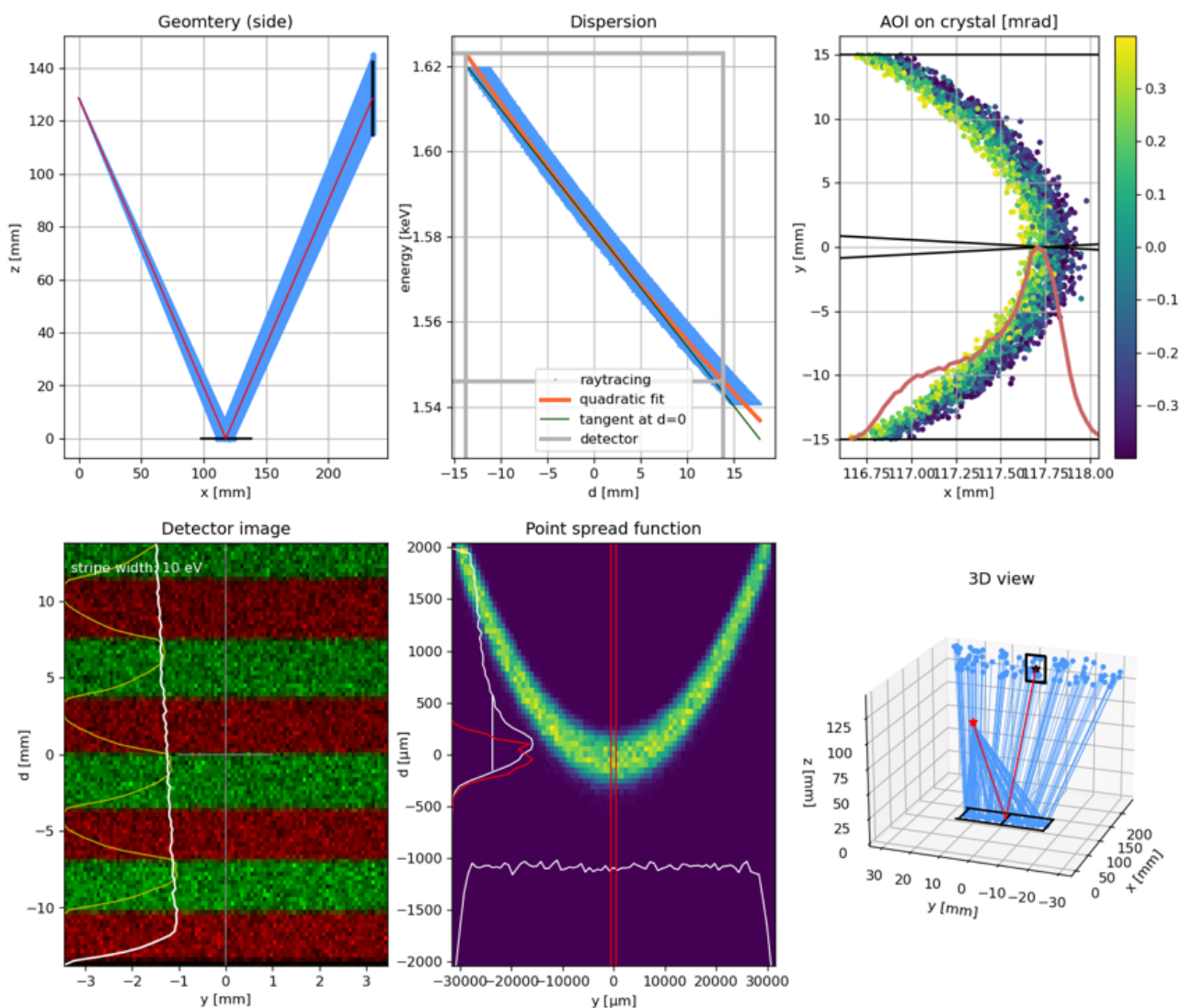


Figure II.4.: Graphical results of mmpxrt simulation of the DUCC, wherein the point spread function used to find the energy resolution is in the bottom middle.

Mmpxrt v. 1.13

DUCC Spectrometer

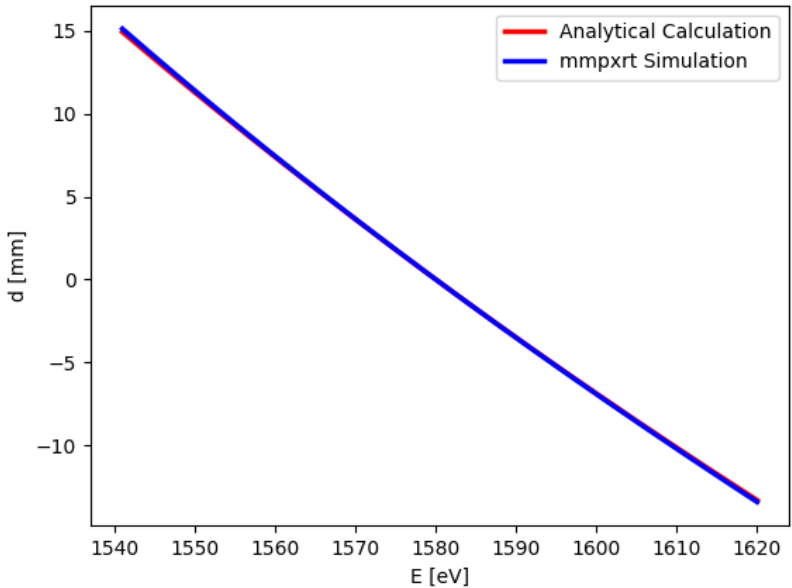
Energy range
 central E: 1580 eV
 E range max.: 79 eV
 i.e. reflecting rays in range: 1541 - 1620 eV
 E range fwhm: 75 eV
 E range on detector: 77 eV

$$\text{dispersion: } E[\text{eV}] = 0.01402d^2 + 2.79d + 1582$$

Energy resolution
 vertical spread from rms: 1.516 mm
 - energy resolution: 4.224 eV
 vertical spread from fwhm: 0.791 mm
 - energy resolution: 2.204 eV
 vert. spr. narrow (fwhm) : 0.341 mm
 - energy resolution: 0.952 eV
 dispersion per px: 0.0 eV/px

Source size broadening
 magnification in spectral direction: 1.48
 source size broadening: 4.14 eV/mm

(a) Numerical results of mmpxrt simulation of DUCC with some quantities removed for clarity.



(b) Dispersion of the DUCC calculated with two different methods.

Figure II.5.: (a): Results of simulation of the DUCC with the parameters as in table 4.1. Simulated using mmpxrt [44]. (b): Comparison of dispersion calculated analytically and through the mmpxrt simulation.

As before, the dispersion $d(E)$ is determined using different methods, namely by the simulation and analytically using eq. 3.8. The results are pictured in fig. II.5b, where again a very good agreement is apparent. In this case the dispersion is also approximately linear, albeit less than for the FSSR-1D, with a fit of the analytical equation resulting in

$$d(E) = 6.306 \cdot 10^{-4} \text{ mm/eV}^2 \cdot E^2 - 2.35 \text{ mm/eV} \cdot E - 2139 \text{ mm} + \mathcal{O}(E^3). \quad (\text{II.3})$$

The energy range as well shows good agreement, with ranges of 1541 - 1618 eV for the simulation and approximately 1541 - 1620 eV for the design. The dispersion per pixel is also as expected, with 0.037 eV/pixel for the analytical dispersion taking into account the pixel size of 13.5 μm , which is low enough to display as 0.0 eV/pixel in the simulation.

In the case of the source broadening, the simulation results slightly deviate from the analytically estimated value. This estimate assumes a source size in the dispersive plane of 150 μm and uses 1-to-1 imaging of a 2D source onto the detector, which follows from the geometry and the fact that source extension in the vertical direction should not affect spectral resolution. Together with the dispersion, this delivers a broadening of 0.592 eV, while the simulation gives a value of 4.14 eV/mm \cdot 0.15 mm = 0.621 eV. The deviation can be possibly traced back to the way that mmpxrt handles the source broadening calculation, which is done using a monochromatic ray tracing, where an offset of the source is introduced for some rays [44]. Accordingly, the source broadening becomes dependent on the crystal quality. The artificially increased rocking curve width therefore leads to higher values of the source broadening in the code. Despite this, the simulation value will be carried over, as the estimate is fairly coarse.

For the energy resolution, as opposed to the FSSR-1D, the third value in fig. II.5a is used, as the detector only covers a fraction of the y range in the PSF graph, so that $\Delta E = 0.952$ eV, while the formula to estimate the spectral resolution from the rocking curve width (see eq. II.2) yields $\Delta E_{est} = 0.238$ eV. Due to the artificial increase of $\Delta\theta$ in the simulation, ΔE_{est} will be used instead of ΔE in this work.

iv. Summary of Simulation Results

For both the DUCC and FSSR-1D spectrometers, the mmpxrt simulations yielded results consistent with the analytical calculations, showing very good agreement for the dispersion, dispersion per pixel and energy range, and good agreement for source broadening. The energy resolution agreed well for the FSSR-1D, while the $\Delta E_{crystal}$ from the DUCC simulation is not meaningful due to the artificially increased $\Delta\theta$.

Since one of the main goals of the simulations was assessing the spectral resolution of each spectrometer, I have gathered and presented the contributions to the resolutions in table II.1, along with the total spectral resolution ΔE_{tot} calculated by summing all the results.

It is immediately clear that the crystal properties are the main limiting factor on the resolution for the FSSR-1D, while the DUCC resolution is mostly limited by the source broadening, with a significant, though smaller, contribution from the rocking curve width. Here we see the advantage offered by the ADP crystal in comparison to the mica, in that it delivers better spectral resolution, albeit at the cost of lower integrated reflectivity and worse bendability. These results also indicate that the detector resolution does not limit the overall spectral resolution for either spectrometer. In general, both spectrometers have sufficient spectral resolutions to perform their roles outlined in section 4.2.

Table II.1.: Resolution contributions for the DUCC and FSSR-1D spectrometers. In both cases, the source broadening is taken from mmpxrt and assumes a source size of $150\text{ }\mu\text{m}$, and the detector resolution is calculated from the mmpxrt dispersion and uses a pixel size of $13.5\text{ }\mu\text{m}$. The contribution due to the crystal properties for the DUCC is estimated as described in section iii, while for the FSSR-1D it is taken from mmpxrt's second ΔE value. The total spectral resolution is calculated by using error propagation on the source broadening and crystal properties' resolution, then linearly adding on the detector resolution.

ΔE Contributions	DUCC	FSSR-1D
Source Broadening	0.621 eV	0.014 eV
Detector	0.038 eV	0.143 eV
Crystal Properties	0.238 eV	2.954 eV
Total	0.703 eV	3.097 eV

III. Alignment Procedure for FSSR-1D

The alignment process can be broken down into 5 steps. To note is that parts of the alignment are built into the mechanical design itself, such that manual adjustments are not required. I will touch on these aspects after explaining the procedure.

Essential to the alignment are the four optical stages labeled in fig. III.1. The rotation stage is a PR01/M, the large linear stage a LX10/M, and the tip-tilt stage a KM100B/M from *Thorlabs*. The fine linear stage, a TSDS-1 from *SigmaKoki*, serves to adjust the crystal-pin distance and the tip-tilt stage allows for pointing in step 2.

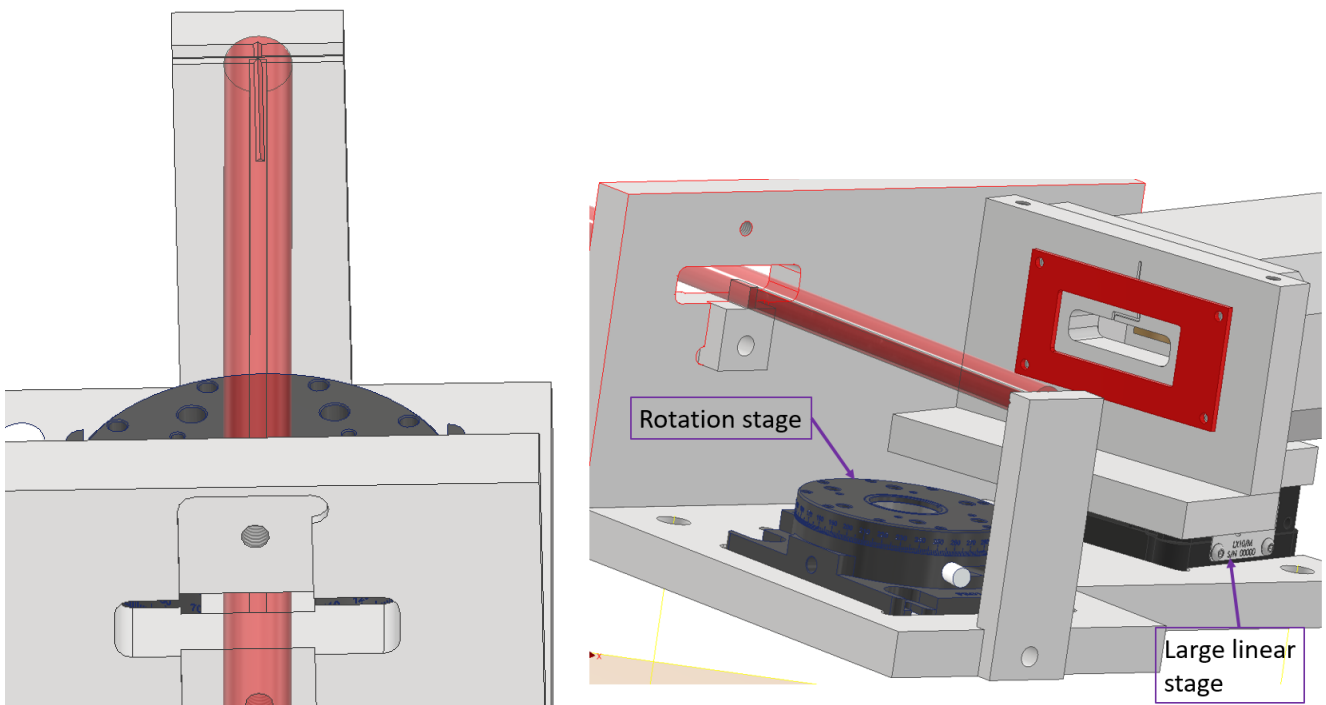
The first three steps are conducted outside the target chamber on an optical table equipped with an expanded collimated laser beam, in our case a HeNe laser, while the last two steps are carried out in the chamber.

1. First, the FSSR-1D without the crystal apparatus is brought into alignment with the HeNe beam for the next steps, simultaneously ensuring that the spectrometer base plate lies parallel to the floor. The HeNe beam is directed onto the opening of the front plate, onto which a pin is affixed, as seen in fig III.1a. The shadow cast by the pin is then aligned with the center of the cross on a plate attached to the back of the base of the FSSR-1D (see fig. III.1b). In this way the beam is parallel to the base plate of the FSSR-1D and to the line drawn out from the pin to the rotation axis of the rotation stage.
2. Now the crystal apparatus, consisting of the rotation stage, fine linear stage, tip-tilt stage and the crystal holder, is put in, as seen in fig. III.1c. Using the fine linear stage and tip-tilt stage, the beam is focused with the crystal onto the surface of the pin (see fig. III.1d), whose distance to the crystal is exactly the focal length of the crystal. This serves to set the location of the Rowland circle and ensure that the crystal center intersects the rotation axis of the rotation stage. It also corrects for any unintended tilts or shifts of the crystal w.r.t the rest of the spectrometer.
3. Next, the central Bragg angle is set by rotating the crystal with the rotation stage. This step leaves the crystal in its final position (see fig. 5.4). In preparation for the next step, the pin is removed and the pointer holder shown in fig. III.2 is attached to the front of the front plate. Analogously to the DUCC, an optical post is set to the required distance and screwed onto the pointer holder.
4. The pointer is then used to orientate the FSSR-1D in the chamber. This is equivalent to fixing the a_0 distance as defined in section 3.2.2.
5. Finally, a laser is shone onto the tip of a needle placed at the TCC. This allows for taking images of the source with photons in the optical range being reflected on the crystal and detected by the CCD camera of the FSSR-1D. By adjusting the distance from chip to crystal using the large linear stage under the camera pictured in fig. III.1b, the position of best focus is found, resulting in the thinnest possible horizontal line on the camera. This is paramount to setting the b_0 distance for the FSSR-1D geometry.

With this the alignment is complete and the FSSR-1D geometry is realized. The most important mechanical details that assist in the alignment are as follows:

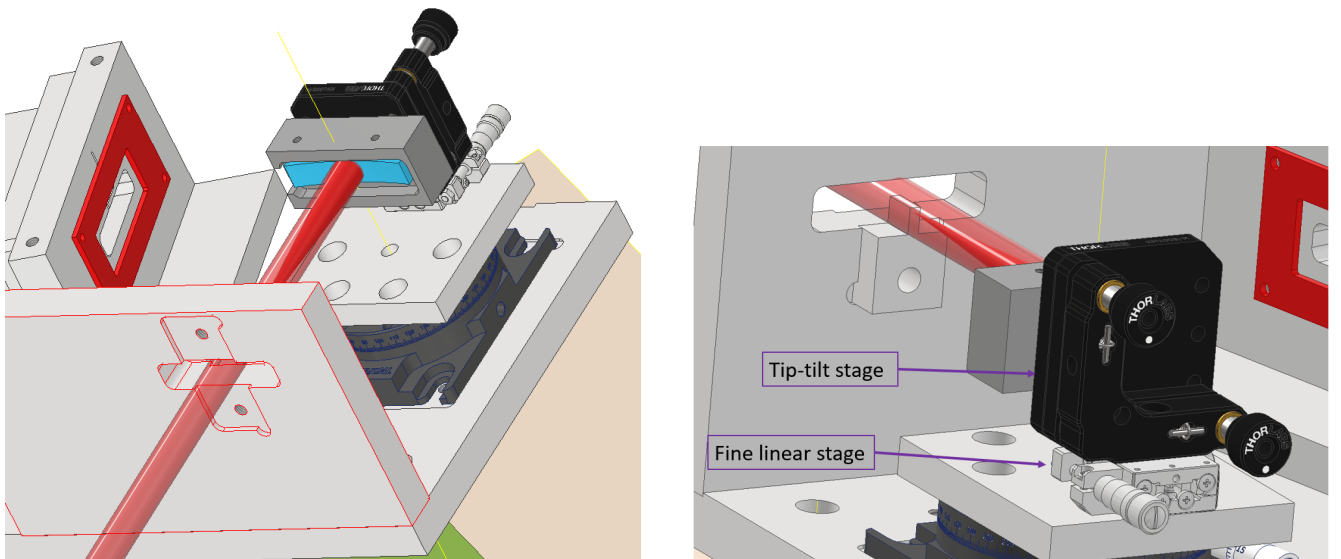
- The rotation stage, front plate, cross plate (used in the first step) and camera linear stage all lie in grooves in the base plate, which fixes their locations and angles w.r.t one another.
- Through additional positioning grooves for the pin and pointer holder, the relative distances between every part is further preserved by mechanical precision. In this way the distance from pin to rotation axis of the rotation stage is set to the focal length of the spherical crystal, allowing the second alignment step to line up the crystal center with the rotation axis.
- Finally, the crystal holder and corresponding connections to the stages ensure that the crystal lies at the correct height and parallel to the base plate, carrying over the alignment achieved in the first step.

With this setup the error of the alignment is mostly limited to mechanical precision, excepting the fourth step, which relies on bare-eye precision. Despite this the overall precision remains excellent, as this uncertainty occurs relatively far from the spectrometer itself, reducing its impact.



(a) Top view of step 1. The HeNe beam is directed through the front plate opening onto the cross plate.

(b) Back view of step 1, where the shadow of the pin is visible in the HeNe beam. The rotation stage and large linear stage are labeled.



(c) Front view of focusing in step 2. The focused HeNe beam is depicted within the main beam in a darker red. The rotation axis of the rotation stage is also shown.

(d) Back view of focusing in step 2. The tip-tilt and fine linear stage are labeled.

Figure III.1.: Model depicting the alignment process for the FSSR-1D using a collimated HeNe laser, which is shown in red. The various optical stages are labeled.

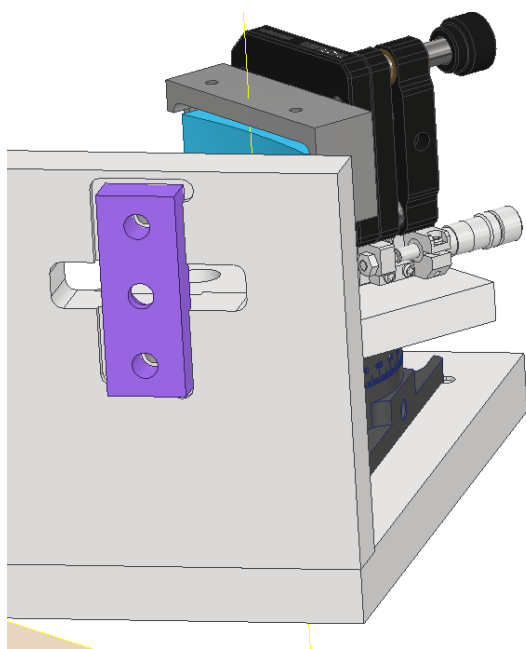


Figure III.2.: Front view of step 3 depicting the pointer holder set in its groove in purple.